Where Are the Missing Baryons in Clusters?

Bilhuda Rasheed

Adviser: Dr. Neta Bahcall

Submitted in partial fulfillment

of the requirements for the degree of

Bachelor of Arts

Department of Astrophysical Sciences

Princeton University

May 2010

I hereby declare that I am the sole author of this thesis.

I authorize Princeton University to lend this thesis to other institutions or individuals for the purpose of scholarly research.

_____

Bilhuda Rasheed

I further authorize Princeton University to reproduce this thesis by photocopying or by other means, in total or in part, at the request of other institutions or individuals for the purpose of scholarly research.

_____

Bilhuda Rasheed

Abstract

We address previous claims that the baryon fraction in clusters is significantly below the cosmic value of the baryon fraction as determined from WMAP 7-year results. We use X-ray and SZ observations to determine the slope of the gas density profile to R_{200}. This is shallower than the slope of total mass density (NFW) profile. We use the gas density slope to extrapolate the X-ray observations of gas fraction at R_{500} to the virial radius (R_{100}). The gas fraction increases beyond R_{500} for all cluster masses. We add the stellar fraction as determined from COSMOS and 2MASS samples, with ICL contributing 10% to the stellar fraction. For massive clusters ($M_{500} \sim 7 \times 10^{14} M_{\odot}$), the baryon fraction reaches the cosmic baryon fraction at $R_{vir} \pm$ 20%. Poorer clusters and groups typically reach 75–85% of the cosmic baryon fraction at the virial radius. We compare these results with simulations which take into account gravitational shock-heating, star formation, heating from SNe and AGN, and energy transfer from dark matter. We find that simulations explain the observed baryon fraction in low-mass clusters but underpredict the baryon fraction in massive clusters.

Acknowledgements

I acknowledge Neta Bahcall as the perfect teacher and guide. I offer my warmest thanks for her undivided attention for many hours every week, her infectious enthusiasm, for rescuing me from countless deadlocks, patiently teaching me how science is done, explaining the same thing a dozen times, working with my limitations and constraints, offering delightfully simple solutions, poring over my draft, being right every time, and for offering me to continue to work with her. She has influenced me both as a scholar and as a person. I also want to thank Paul Bode for taking the time to entertain my repeated requests to run his model over and over again, and for offering many valuable insights. Many thanks to Courtney Dressing for being the most knowledgeable and helpful workmate possible. Thanks to all the Astro undergrads for making the office a fun place to be. Thanks to Michael Strauss for agreeing to be my second reader. I also thank Rachel Mandelbaum, Gregory Novak, Xenia Morin, Matt George, Eric Hallman and Alexey Vikhlinin for responding to my queries.

Contents

Chapter 1

Introduction

1.1 The Problem of Missing Baryons in Clusters

Rich clusters of galaxies—families of hundreds of galaxies held together by the gravitational potential of the cluster—are the most massive systems which have had time to undergo gravitational collapse and virialization in the history of the Universe. As such, clusters of galaxies serve as powerful tools in constraining the cosmological model of the universe. Cluster masses typically range from 10^{14} to 10^{15} solar masses ($M_{\odot}$). Ranging from poor clusters to rich, they contain between 10 and 100 typical (L^*) galaxies each. They stretch from 2–4 Mpc and their velocity dispersions are 500–1200 km/s.

Clusters have three major components: a dark matter halo; hot gas in between galaxies which is at such high temperatures ($10^7 - 10^8$K) that it emits X-ray bremmstrahlung radiation; and stars, mostly found in galaxies, which have formed from cooled gas. The gas and the stars collectively constitute 'baryons', i.e., normal matter. We have observationally determined that most of the cluster mass is dark ($\sim 83 - 90\%$). Of the baryonic matter, most of it is gas ($\sim 14\%$ of cluster mass). Stars are only $\sim 2\%$ of cluster mass, indicating that only a small percentage of the

intracluster gas has cooled to form galaxies.

How do we detect each of these components? Only the baryonic matter (gas and stars) is luminous. We observe the gas primarily via X-ray telescopes (notably, Rosat, Chandra and XMM-Newton). Clusters are prominent X-ray sources in the sky. In addition, gas can be detected indirectly by observing its effect on the cosmic microwave background (CMB) radiation. The interactions of the CMB with hot electrons in the intracluster gas (ICM) produce a decrement in the CMB signal, called the Sunyaev-Zel'dovich effect. This effect yields a measure of the gas thermal pressure, which is the product of density and temperature of the intracluster gas.

The stellar mass in galaxies can be measured by measuring the optical (K-band) luminosity of the galaxies in the cluster, and then fitting it with standard spectra of stars in order to find what stellar types inhabit the galaxies. Then the stellar mass is estimated by using the mass-to-light (M/L^*) ratios of those stars. The intergalactic stars are few and produce diffuse intracluster light (ICL), which is detected by near infrared photometry. The ICL is only about 10–20% of the stellar mass in galaxies, and thus a very small portion of the total cluster mass.

The distribution of the total matter of the cluster, including dark matter, can be found most accurately from gravitational lensing. The deep gravitational potential wells of massive clusters generate shape distortions in the images of background sources due to differential deflection of light rays. Reliable measurements of weak lensing are now available (e.g., Mandelbaum et al. [2008], Zhang et al. [2008], Umetsu et al. [2009], and references therein). Less reliable methods to find the total mass profile of clusters are hydrostatic equilibrium, velocity dispersion and temperature-scaling relations. Hydrostatic equilibrium assumes that gravitational energy in clusters is balanced by thermal pressure. The assumption of hydrostatic equilibrium allows X-ray data to be used to estimate cluster mass (e.g.,Vikhlinin et al. [2006], Arnaud et al. [2007], Sun et al. [2009]), since X-ray data gives a measure of gas density as well as gas

temperature which together produce thermal pressure. However, this method usually leads to an underestimate of mass, since non-thermal pressure may also exist (e.g., Nagai et al. [2007] and references therein). Similarly, virial equilibrium assumes a balance between kinetic and potential energies in a cluster. Thus the total mass of the cluster can be estimated as $\sim \sigma^2 R/G$, where σ is the velocity dispersion of the cluster, R radius from the center and G the gravitational constant. The temperature-scaling method assumes self-similarity in clusters and estimates the mass of a cluster from its observed X-ray temperature, using the mass-temperature (or mass-luminosity) relations found by lensing from a large sample of clusters (e.g., Bahcall [1977], Finoguenov et al. [2001], Pratt et al. [2009], and references therein).

In a hierarchical structure formation formation of the universe, the size of clusters implies that their contents have accreted from regions of 8–40 comoving Mpc. This big a piece of the universe can be expected to be representative of the mean matter content of the universe. While clusters started out with the mean matter content of the universe, it further helps that clusters are extremely massive ($10^{14}-10^{15} M_{\odot}$) which gives them enormous gravitational binding energy. Therefore, clusters are expected to retain their gaseous matter over time. Despite the presence of huge energy sources such as supernovae and active galactic nuclei (AGN), as well as gravitational shock-heating (Takizawa and Mineshige [1998] and references therein), such heat sources should not be able to separate baryons and dark matter on the scales of several megaparsecs. Therefore, it is commonly expected that clusters retain the same baryon fraction today as they started with, i.e., the universal fraction. In contrast, smaller systems such as galaxies have neither the size to be representative of the universe, nor the gravity to retain all their gas. Clusters are important because the ratio of baryonic mass to dark mass in clusters should reflect the universal ratio of baryonic matter to dark matter, because of the size and depth of their gravitational potential

wells.

This property of clusters has proved very useful for cosmology. In the 1990's, a big question in cosmology was whether the matter density of the Universe (Ω_m) is 1 or lower. $\Omega_m = \rho_m/\rho_{crit}$ is the ratio of the total matter density in the universe, baryonic and dark, to the critical density of the universe. The critical density refers to the density needed for a flat (no curvature) universe. So a flat universe would have $\Omega_m = 1$, unless there is another component besides matter. It was not known whether the universe is flat, or whether there is another component to it.

In addition, Big Bang nucleosynthesis (BBN) had been used to determine the baryon density of the present universe ($\Omega_b = \rho_b/\rho_{crit}$) which provided another piece of the puzzle. The relative abundances of the light elements, ^{1}H, ^{2}H, ^{3}He, ^{4}He and ^{7}Li, combined with BBN theory nicely constrain the total baryon density of the Universe (Walker et al. [1991]). Baryon densities much larger than a certain value would overproduce both ^{4}He and ^{7}Li, whereas significantly smaller values would overproduce both ^{2}H and ^{3}He. The value for Ω_b from big bang nucleosynthesis has been determined to be $0.02h^{-2}$ (Burles and Tytler [1996] and references therein), or ≈ 0.04 if $h \approx 0.7$.

In the 1990's, improved observations indicated with increasing confidence that the total matter density of the universe $\Omega_m \sim 0.2$ (Bahcall et al. [1995], White et al. [1993], Bahcall and Fan [1998], Carlberg et al. [1996]). A decisive argument in this debate was White et al. [1993]'s, who showed that the baryon fraction (Ω_b/Ω_m) measured in rich clusters was inconsistent with $\Omega_m = 1$. They used new X-ray data from Rosat and the Einstein observatory to estimate the gas mass in clusters (White et al. [1993], White and Fabian [1995]). They found stellar mass from M/L ratios and total mass from velocity dispersions. Thus, they found the mean baryon fraction for their clusters:

$$f^b \equiv \frac{\Omega_b}{\Omega_m} = \frac{M_{baryons}}{M_{total}} \geq 0.07h^{-3/2} + 0.03 \tag{1.1}$$

This comes out to be $\Omega_b/\Omega_m \approx 0.15$ if $h \approx 0.7$. If $\Omega_b \approx 0.04$ from nucleosynthesis, and $\Omega_b/\Omega_m = 0.15$, then under the expectation that clusters are a good representation of the universe, White et al. [1993] were seeing far too many baryons in clusters than allowed in a universe with $\Omega_m = 1$. Unable to determine a mechanism for such dramatic baryon enhancement in clusters, they concluded that $\Omega_m \approx 0.27$. This value had been independently found by other methods (see references above), and is indeed the current best value for the matter density of the universe.

This discrepancy between $\Omega_b = 0.04$ and $\Omega_m = 0.27$ was what led to the requirement of non-baryonic, 'dark' matter. In fact, the richest clusters of galaxies most strongly pointed to the existence of dark matter. As early as 1933, Fritz Zwicky observed the velocity dispersion of the Coma cluster, and used the virial theorem to estimate the mass of the cluster. The virial theorem predicts that the cluster mass is roughly proportional to the square of the velocity dispersion. The mass Zwicky derived from the virial theorem was much larger than expected from the luminosity of the galaxies within the cluster. On the basis of this result he predicted the presence of undetected dark matter in clusters (Zwicky [1937]), which was confirmed much later.

Over the past decade, dramatic progress has been made in observations of all the main components of clusters. Deep high-resolution wide-field imaging has vastly improved the accuracy of strong and weak lensing measurements, which tell us about cluster mass profiles (e.g., Zhang et al. [2008], Mandelbaum et al. [2008]). Deep imaging in multiple optical bands as well as in the near infrared has permitted a systematic census of the stellar components in clusters (e.g., Lin et al. [2003], Gonzalez et al. [2007], Andreon [2010], Giodini et al. [2009]), including the diffuse intracluster light Zibetti [2008], Gonzalez et al. [2005]. High resolution, sensitive X-ray observations by

Chandra and XMM-Newton have revolutionized our knowledge of the properties of the hot intracluster gas by reliably mapping gas density, temperature and metallicity out to radii of R_{500} (e.g., Vikhlinin et al. [2006], Arnaud et al. [2007], Sun et al. [2009]) and in some cases to R_{200} (Ettori and Balestra [2009], Bautz et al. [2009], Plagge et al. [2009]) (where R_{500} and R_{200} refer to the radii at which the cluster mass density is 500 and 200 times the critical density of the universe, respectively). Sunyaev Zel'dovich measurements of gas pressure have also been recently done (Plagge et al. [2009], Afshordi et al. [2007]). These improved observations of cluster components have led to better constraints on the universal ratio of baryons to total matter (e.g., David et al. [1995], Evrard [1997], Allen et al. [2002], and references therein).

The last decade has also seen the advent of cosmic microwave background (CMB) cosmology, especially with the *Wilkinson Microwave Anisotropy Survey* or the WMAP. The length scale of fluctuations in the primordial power spectrum constrains the value of Ω_m. The height of the peaks in the power spectrum also constrains Ω_b. Therefore, the CMB provides with an independent, precise and accurate measurement of the universal baryon fraction $f^b \equiv \Omega_b/\Omega_m$. The most recent value of f^b from WMAP 7-year results is 0.1675 ± 0.006 (Jarosik et al. [2010]).

This has raised a puzzle. The most recent and best observations from Chandra and XMM-Newton indicate that cluster gas fractions are below the WMAP value of the cosmic baryon fraction. The best estimates of stellar mass do not account for the discrepancy. This gave rise to the problem of "missing baryons". For example, Chandra (Vikhlinin et al. [2006]) and XMM-Newton (Arnaud et al. [2007]) measurements constrain f^{gas} in the most massive clusters ($\sim 10^{15} M_\odot$) at 0.123 ± 0.007. This is $73 \pm 4\%$ of the WMAP value of the cosmic baryon fraction. Mean gas fraction for less massive clusters has been observed to be even lower (Sun et al. [2009]). K-band luminosity analysis of galactic stars and near infrared observations of intergalactic

stars have put the stellar fraction for this rich class of clusters at 0.020 ± 0.002 (Lin et al. [2003], Giodini et al. [2009], Zibetti [2008]). Taken together, the baryon fraction becomes 0.143 ± 0.007 for massive clusters with $M \sim 10^{15} M_{\odot}$, or $85 \pm 4\%$ of the cosmic baryon fraction as measured from WMAP 7-year results.

Other measurements, for instance by Umetsu et al. [2009] using gravitational lensing to find total mass and the AMiBA telescope for Sunyaev-Zeldovich measurements, find the sample average f^{gas} for their four clusters to be 0.133 ± 0.027. This is $78 \pm 16\%$ of the WMAP value of the cosmic baryon fraction. Yet others such as Afshordi et al. [2007, 2005] find an even larger shortfall in cluster gas fraction in comparison with WMAP results. Afshordi et al. [2007] used Sunyaev-Zel'dovich measurements from WMAP itself to estimate thermal pressure in the ICM. They use cataloged X-ray temperatures of clusters to estimate the thermal energy of their clusters, which is significantly lower than if all the baryons were in the hot ICM phase. They estimate $f^{gas} = 0.109 \pm 0.013$ at R_{200}, which is only $65 \pm 8\%$ of the cosmic baryon fraction. Since stars contribute no more than 15% to total baryons, Afshordi et al. [2007] have claimed that $\sim 35\%$ of the baryons in clusters are "missing", which they present as a big puzzle to the astrophysical community.

The problem of the missing baryons has important implications for Astrophysics. It affects the correct cosmological model for our universe. The current baryon fraction in clusters sheds light on the thermodynamics and energetics accompanying the growth of large-scale structure. It will put important constraints on the gravitational and non-gravitational energy sources in groups and clusters. In addition, if it turns out that galactic heat sources such as active galactic nuclei (AGN) significantly heat up the ICM, it would shed light on the unresolved question of galaxy formation and the efficiency of gas cooling into stars. These are all big questions in astrophysics which are not yet understood and which are difficult to observe or constrain by other means. In Chapter 4 we will attempt to explain our results for the baryon fraction in

groups and clusters in light of currently proposed theories of cluster energetics, and it will be clear that these theories are at an early stage of development and as yet insufficient to explain all the findings.

Afshordi et al. [2007] propose that the "missing baryons" are most probably hiding in some cold, undetected form in the intracluster medium. This is to avoid the conclusion that clusters actually deviate dramatically from the universal baryon fraction and have a severe baryon deficit. That would be a troubling proposition, given that the clusters accreted from scales of 8–40 Mpc, and have enormous gravitational binding energy.

Some have even proposed revising Ω_m upwards once again, since no mechanisms can conceivably lower the cluster baryon fraction so significantly below the cosmic value. A more likely solution, they suggest, is that the WMAP systematically underestimates Ω_m (see McCarthy et al. [2007]).

1.2 A Proposed Solution

Our solution is based on the hypothesis that, even as various heat sources cause the intracluster gas to spread outward from the center, the cluster is so massive that the gas can nevertheless be located if we look to large enough radii. As gas accretes from a radius of tens of megaparsecs, it collides with the inner shells of gas already present—a bit like two balls falling vertically, one on top of the other. This collision converts the gravitational potential energy of accreting gas into heat and sends a shock-wave outward through the gas halo (Takizawa and Mineshige [1998] and references therein). The shock waves cause the gas to expand outward. The extra heat in the gas halo disturbs the hydrostatic equilibrium in the outskirts of the cluster. Cold dark matter, being collisionless, does not experience shock heating. The result is that the hot gas distribution is more "spread out" than the dark matter halo. This is indeed observed

(e.g., Vikhlinin et al. [2006], Pratt et al. [2006], Ettori and Balestra [2009], Plagge et al. [2009], etc.) and predicted from simulations.

See Figure 1.1 as an example. This figure has been taken from Vikhlinin et al. [2006] who measured the gas and total mass profiles of 13 clusters using Chandra. On a logarithmic scale, the gas profile is shallower or less concentrated at large radii than the total mass profile which includes gas and dark matter. (The stellar mass profile follows the total mass profile to a good approximation.) Since total mass density falls off more steeply than the gas density, the result is that *the fraction of gas mass over total mass contained within a certain radius increases with radius.* Vikhlinin et al. [2006] observed that although the gas fraction did not reach the cosmic value, the gas fraction was still increasing to the largest radius observed (R_{500}) in all the clusters.

My solution draws from this observation, confirmed by other sources (Arnaud et al. [2007], Pratt et al. [2006], Plagge et al. [2009], Ettori and Balestra [2009], and references therein). Since the gas has been observed to be more widely distributed in clusters than the dark matter, it follows that if we manage to extend our observations to larger radii than previously observed, we may be able to locate the "missing baryons" in clusters. The expectation is that the gas fraction will increase as we go to larger radii than previously observed, causing the baryon fraction to also increase with radius (even as the stellar fraction stays the same). In simple words, if the gas was driven outward by miscellaneous heating mechanisms, it should nevertheless reside at large radii. Seeing the missing gas is only a matter of looking far enough.

It would be useful, then, to see whether this effect can potentially solve the problem of low baryon fraction in clusters, i.e., whether the cluster baryon fraction can rise to match the cosmic baryon fraction if we account for the gas residing unexplored at cluster outskirts. It would also be interesting to investigate whether this can be achieved for only the most massive clusters or the full mass range from groups to clusters. At stake is our understanding of the energetics and dynamics of cluster

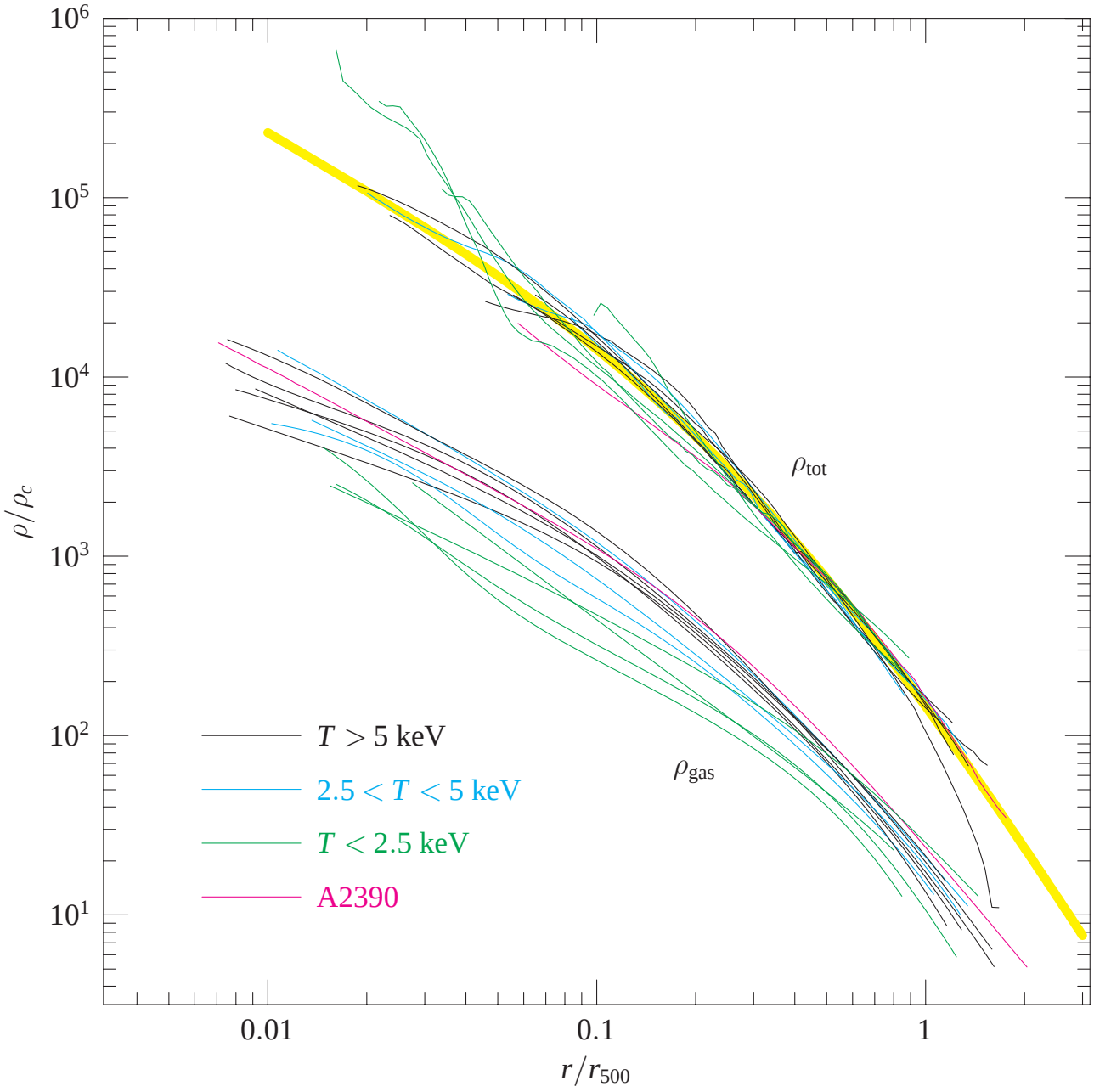

Figure 1.1: Density profiles (scaled to the critical density) for the Chandra clusters observed by Vikhlinin et al. [2006]. The total matter density (including baryonic and dark) falls off more steeply than the gas density profile at large radii, so that the fraction of gas mass over total mass increases with radius. It is found increasing at the outermost radii observed (R_{500}). The dark lines show the most massive clusters. The yellow line is for comparison with the theoretical NFW profile (Section 2.1, Navarro et al. [1996]) with $c_{500} = 3$, which fits very well to the observed total mass profiles.

formation. The simplest expectation is that massive clusters retain their baryon fraction. If it turns out that the "problem of missing baryons" is just a matter of incomplete observations, then any major changes in the theories of gravitational accretion and energy inputs in clusters will be obviated. It would redeem the clusters as representative of the mean matter content of the universe.

To make these ideas more concrete, we will introduce the convention for radius calibration in virialized systems. The 'virial radius' is the radius within which virial equilibrium holds, i.e., gravitational potential energy is balanced by kinetic energy, so that no further collapse takes place and the system has a stable size. From non-linear theory of growth of structure, we can derive the particular value of the *density contrast*, Δ, which characterizes virialization. By 'density contrast' we mean the ratio of the mean density of an 'overdense' region undergoing collapse, to the mean density of the background universe. As an overdense region collapses, its density increases. For a high enough value of Δ, i.e., when a region attains a certain value of overdensity with respect to the universe surrounding it, the region is predicted to *virialize*, i.e., become pressure-supported and stable in size. After virialization is achieved, the density of the system, or Δ, stays essentially constant over time (or redshift). Non-linear theory tells us that, for a matter-only universe ($\Omega_M = 1$), $\Delta_{vir} = 178$. However, for our lightweight, flat universe with low matter density and vacuum energy, Δ_{vir} is given by (Bryan and Norman [1998], Eke et al. [1998]):

$$\Delta_{vir} \equiv \frac{\rho_{vir}}{\rho_{crit}} = 178[\Omega_m^{0.45}] \tag{1.2}$$

This formula is accurate to within 5% for $0.15 < \Omega_m < 1$. (For a derivation, see Eke et al. [1998].) Taking $0.26 < \Omega_m < 0.30$, we get $97 < \Delta_{vir} < 103$. So for this paper we will take $\Delta_{vir} \approx 100$.

Recall that matter density in a cluster is high at the core and falls off with radius.

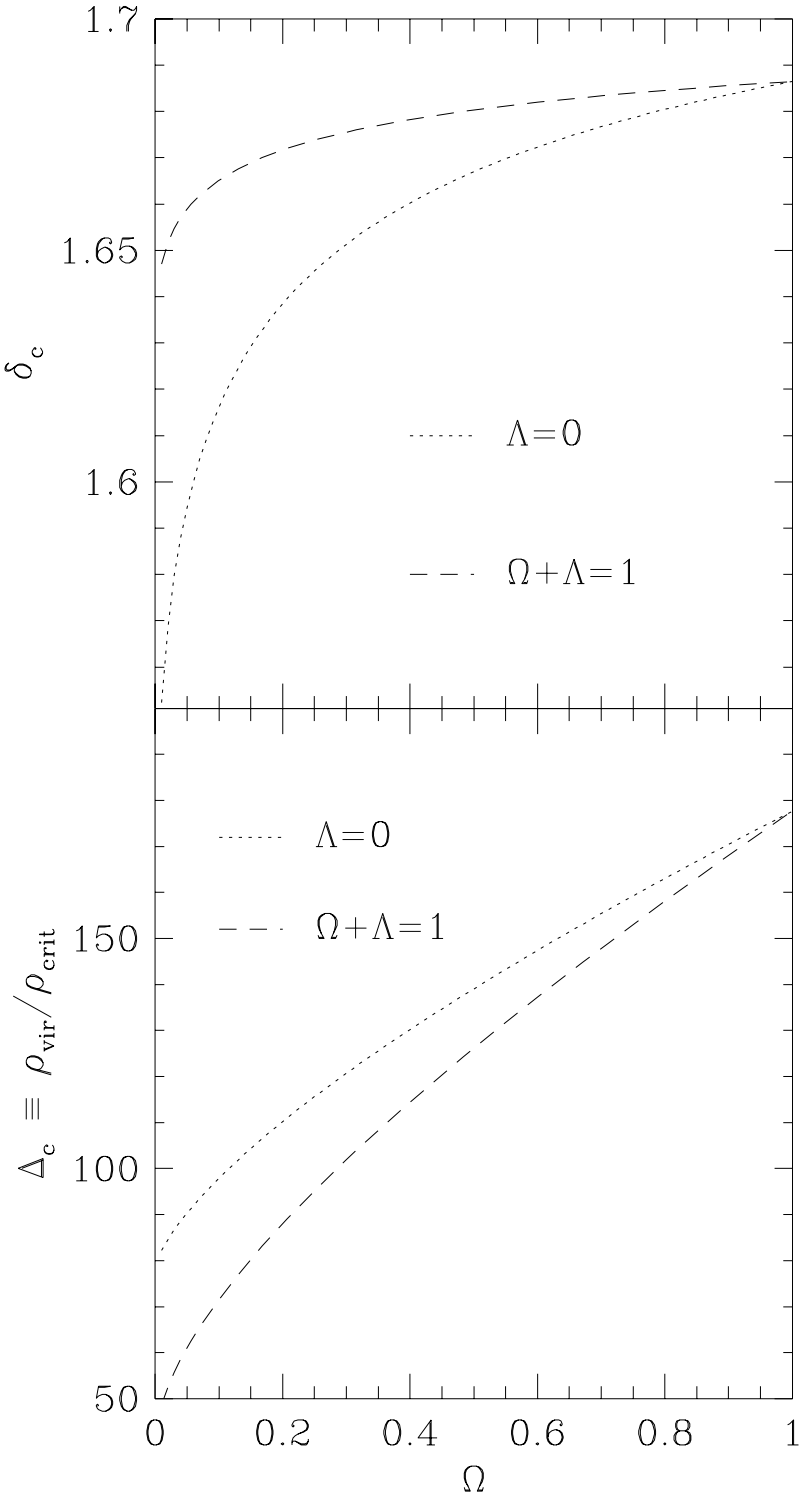

Figure 1.2: Upper panel: Critical threshold for collapse, δ_c, from linear theory of spherical collapse. Lower panel: the virial density of collapsed objects in units of critical density from non-linear theory. Source: Eke et al. [1996]

Since mass is concentrated at the center, it follows that if the density contrast Δ (total matter contained within that radius over volume) is 100 within the virial radius, it must have a higher value within a radius smaller than the virial radius. Using this observation, we denote cluster radii by the density contrasts they represent with respect to the critical density of the universe. Near the core, the density of a cluster can be a few thousand times the critical density. As radius becomes larger, density contrast becomes smaller, until it is ≈ 100 at R_{vir}. At outer radii, in which we are interested, the following density contrasts (or equivalently, radii) are used as important observational benchmarks: R_{500}, R_{200} and R_{100}, the radii within which the density contrast with the critical density of the universe is 500, 200, and 100, respectively. Thus, R_{500} is smaller than R_{200} which is smaller than R_{100}. R_{100} is taken to be equal to R_{vir}, as we explained above. Similarly, M_{500} is the mass within R_{500}, or $500\rho_{crit}(4\pi/3)R_{500}^3$. M_{200} is naturally larger than M_{500}, and so on.

Observations and simulations show that clusters are largely self-similar in terms of total mass density profiles, such that the density profiles of all clusters can be well-described by a universal formula (see Section 2.1, Navarro et al. [1995, 1996]. For instance, see the yellow line in Figure 1.1, which all clusters in the sample nicely conform to.) One result of this useful self-similarity of clusters is that the ratios between R_{500}, R_{200} and R_{vir} are more or less constant for all clusters: $R_{500} \approx 0.7R_{200}$, $R_{100} \approx 1.3R_{200}$. Thus the virial radius corresponds to approximately twice R_{500}. We will use these ratios later in our analysis.

With the advent of Chandra and XMM-Newton, it has become possible to detect cluster gas density in many cases to R_{500}. In some cases, observations have been made to R_{200}. In other words, even the most recent cutting-edge observations only go to roughly half, or at most three quarters, of the virial radius. This observational limitation arises because the gas density at such large radii becomes too low to emit easily detectable X-ray signal.

This fact allows us to put the claims of "missing baryons in clusters" in context. In the previous section we listed a few papers which have claimed to see less baryons in clusters than expected. However, Vikhlinin et al. [2006] and Arnaud et al. [2007], using Chandra and XMM-Newton respectively, collect data only to R_{500}, or half the virial radius. It should perhaps be no surprise that their baryon fraction falls short of the cosmic value at this radius. The gas fraction f^{gas} is clearly rising at the outermost radii observed. We should allow, therefore, for the extrapolation of the baryon fraction to larger radii to see if it can be reconciled with the cosmic baryon fraction at closer to the virial radius.

Afshordi et al. [2007] see a lower value of f^{gas} than Vikhlinin et al. [2006] and Arnaud et al. [2007] even as they observe to R_{200}. One reason might be that their sample of 193 clusters ranges in mass from poor clusters to rich, unlike the samples of Vikhlinin et al. [2006] and Arnaud et al. [2007] which comprise of rich clusters only. It could be that the baryon fraction varies with total mass, and the most massive clusters have a higher baryon fraction than less massive clusters. Our analysis investigates this question as well.

In this paper, we will use the most recent and best observations of cluster gas density and total mass density to (i) determine the best value of the gas fraction at R_{500}; (ii) determine from observations how the *slope* of the gas density and the total density profiles varies in the range of R_{500} to R_{vir}; and (iii) use the 'baseline' baryon fraction observed at R_{500} and the slopes of the density profiles to extrapolate the baryon fraction to the virial radius. We will also explore the variation of the baryon fraction with mass, at R_{500} and beyond.

In Chapter 2 we present the observations which form the basis for our 'baseline' data at R_{500}: the gas fraction, stellar fraction, total mass, total density slope and gas density slope for various masses of clusters; in Chapter 3 we use observations to extrapolate the baryon fraction at R_{500} to R_{200} and R_{100} (the virial radius); in Chapter

4 we discuss our results in terms of cluster energetics and dynamics; in Chapter 5 we compare the results of our extrapolation with observations of the gas fraction at R_{200}; and in Chapter 6 we give a summary and our conclusions. The cosmology assumed throughout is a ΛCDM model with $\Omega_m = 0.258$, $\Omega_\Lambda = 0.742$, and $\mathrm{H}_0 = 72$ km/s/Mpc, unless otherwise stated.

Chapter 2

Observational Data

In this chapter we first review some cluster basics: the observed profiles of total density, gas density, galactic stars and ICL at large radii. We then use the most recent and best observations to constrain the baryon fraction at R_{500} as a function of M_{500}. We then use observational data to constrain the slope of the gas density profile verses radius in the region of R_{500} to R_{100}, for the purposes of extrapolation from R_{500} to the virial radius, R_{100}.

2.1 The Universal Mass Density Profile of Groups and Clusters

The distribution of total mass (baryonic and dark) in a cluster (or group) follows a universal density profile, regardless of cluster mass, power spectrum shape, or the value of the cosmological parameters, as shown from both simulations and observations. This universal mass density profile is best described by an analytical model first proposed from simulations by Navarro, Frenk and White (Navarro et al. [1995, 1996], Dubinski and Carlberg [1991]). Observations have repeatedly confirmed the 'NFW' profile, as it is now called, to be the correct description for the mass density profile in

clusters and groups (Mandelbaum et al. [2008], Sheldon et al. [2009], Umetsu et al. [2009] and references therein, also see Figure 1.1). The formula describes the mass density outside the cluster core as an inverse power law with radius, i.e., $\rho(r) \propto r^{-\alpha_m}$, with the slope α_m steepening from ~ -1 near the core to ~ -3 at the outskirts. The full formula is:

$$\rho(r) = \frac{\delta_c \rho_{crit}}{(r/R_s)(1 + r/R_s)^2}, \tag{2.1}$$

where $\rho_{crit} \equiv 3H^2/8\pi G$ is the critical density at the given redshift (H is the corresponding value of the Hubble constant). R_s is a characteristic radius constrained by the concentration parameter of the cluster, which is usually defined as $c_{200} \equiv R_{200}/R_s$. The c_{200} parameter then serves as a comparison of concentrations between clusters. A more concentrated cluster will have a smaller core radius R_s, and thus a larger value of c_{200}. δ_c is the characteristic overdensity of the cluster (see Figure 1.2, upper panel), constrained by the fact that the mean density within R_{200} should be $200 \times \rho_{crit}$.

$$\delta_c = \frac{200}{3} \frac{c^3}{[\ln(1 + c) - c/(1 + c)]} \tag{2.2}$$

From Equation 2.1 we can see that close to the core where $r \sim R_s$, the density falls as $\sim r^{-1}$. At the outermost radii where $r \gg R_s$, density falls as $\sim r^{-3}$. The logarithmic slope of the mass density profile $-\alpha_m \equiv d \log \rho(r)/d \log r$ would then vary from ~ 1 close to the core to ~ 3 at very large radii.

Generally, the value of the concentration parameter c_{200} varies with cluster mass. Our sample of nearby clusters has a mass range from $M_{500} = 3 \times 10^{13} M_\odot$ to $M_{500} = 1 \times 10^{15} M_\odot$. Mandelbaum et al. [2008] use the Sloan Digital Sky Survey to derive a relation between halo mass and concentration from weak lensing. They find that the NFW concentration parameter c_{200} decreases with halo mass, from 10 for galactic

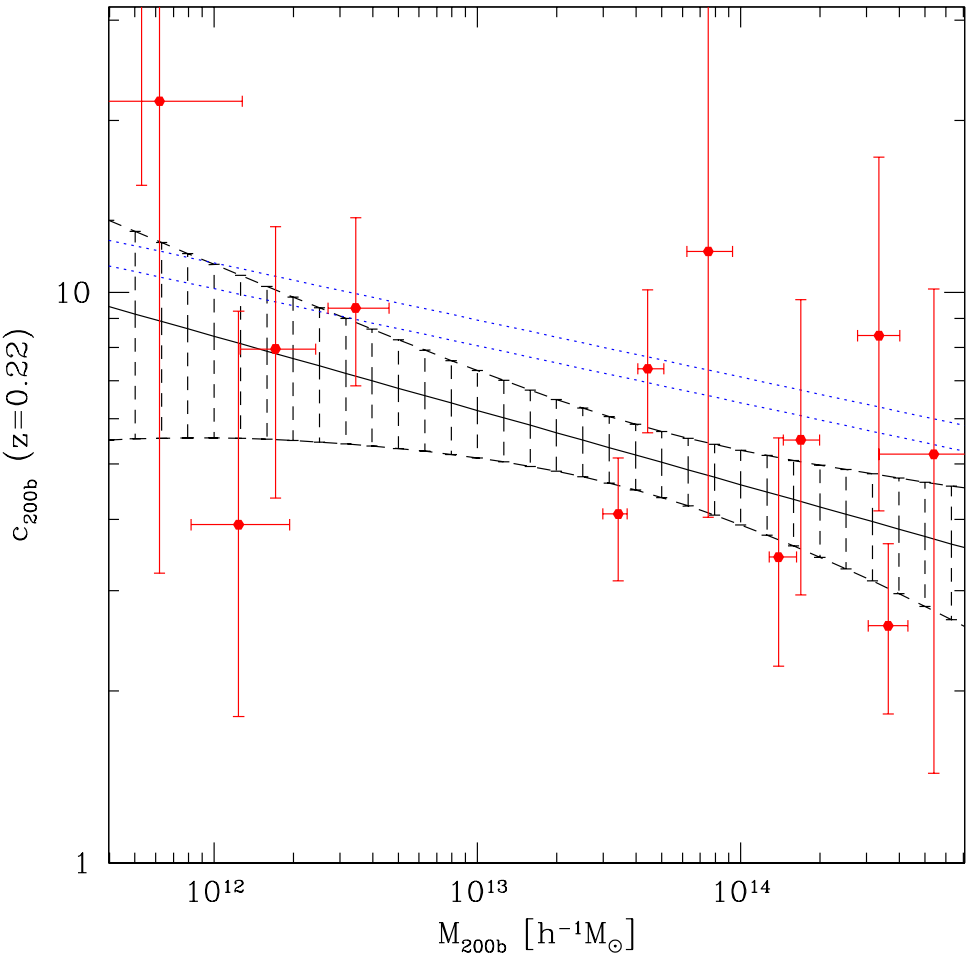

Figure 2.1: The best-fit $c(M)$ relation from Mandelbaum et al. [2008] at $z = .22$, using SDSS weak lensing measurements to map the mass distribution in groups and clusters. The 1σ allowed region is indicated. The red points with error bars show the best-fit masses and concentrations for each bin when fit individually, without requiring a power-law $c(M)$ relation. The blue dotted lines show comparison with simulation results of Neto et al. [2007]. Note that the mass scale is calibrated by M_{200}, whereas in our paper we generally calibrate masses in M_{500}, which is about a factor of 0.85 lower. For our mass range $3.7 \times 10^{13} M_\odot \leq M_{200} \leq 11.7 \times 10^{14}$, Mandelbaum et al. [2008]'s best fit relation gives $c_{200} \approx 5$.

halos to about 4 for massive clusters. They assume a power law dependence of concentration on halo mass in the form of $c_{200} = c_0(M/10^{14}h^{-1}M_\odot)^{-\beta}$, and find best-fit $c_0 = 4.6 \pm 0.7$ and $\beta = 0.13 \pm 0.07$. According to this relation, shown in Figure 2.1, the best fit value of c_{200} for our mass range of $3.2 \times 10^{13}M_\odot \leq M_{500} \leq 10 \times 10^{15}M_\odot$ is ≈ 5. Note that Mandelbaum et al. [2008] give halo mass in terms of M_{200}, whereas we calibrate halo mass as M_{500}. The latter is systematically lower than the former by about a factor of 0.85. This means that on Mandelbaum et al. [2008]'s scale, our cluster sample falls in the range $3.7 \times 10^{13}M_\odot \leq M_{200} \leq 11.7 \times 10^{14}$, corresponding to $c_{200} \approx 5$.

Mandelbaum et al. [2008]'s observational estimates of c_{200} are slightly lower than but within 1σ of results from simulations. For example, the original paper by Navarro et al. [1996] yielded from simulations a concentration parameter $c_{200} \approx 6.5$ for masses of the order of $10^{14}M_\odot$, which agrees within 1σ with Mandelbaum et al. [2008]. More recently, the Millennium simulations of Neto et al. [2007] predict that $c_{200} \approx 4.6$ for this mass range, nicely consistent with observations.

Setting $c_{200} = 5$, we can analytically derive values of the mass density slope $\alpha_m = -d\log\rho(r)/d\log r$ in the the range from R_{500} to R_{100}. We find that $\alpha_m = 2.57$ **in the vicinity of** R_{500}**.** α_m **steepens to** 2.74 **in the vicinity of** R_{100}**.** On average, in the interval between R_{500} and R_{200}, $\alpha_m \approx 2.6$. In the next interval (of roughly equal length) between R_{200} and R_{vir}, α_m averaged to ≈ 2.7.

2.2 The Gas Density Profile

Gas contributes the largest share to baryons in clusters ($\sim 60-90\%$). The gas density profile is observed to be more spread out, or shallower, than the NFW profile (Figure 1.1). Since the gas density profile falls off less steeply than the NFW profile, the gas fraction f^{gas} increases with radius.

The gas density profile is best fitted by a 'beta model' (Cavaliere and Fusco-Femiano [1978] and references therein). Like the NFW profile, the beta model follows an inverse power law behavior of gas density with radius, i.e., $\rho_{gas}(r) \propto r^{-\alpha_{gas}}$. The beta model often fits less well at the core region, and so has to be modified at small radii (e.g., see Vikhlinin et al. [2006]). But we are only concerned with large radii, $r > R_{500}$, where the beta model proves a good fit.

$$\rho_{gas}^2 = n_p n_e = \frac{n_0^2}{(1 + r^2/R_c^2)^{3\beta}} \tag{2.3}$$

where n_p and n_e are the densities of protons and electrons in the intracluster gas, respectively. R_c is the core radius, and $3\beta = \alpha_{gas} = -d\log\rho_{gas}(r)/d\log r$ for $r \gg R_c$. In these terms, the gas density profile is shallower than the NFW profile if $\alpha_{gas} < \alpha_m$.

Below we will describe the observations we used to constrain the behavior of the density profile in the vicinity of R_{500} and beyond.

2.2.1 Chandra Measurements

Vikhlinin et al. [2006] present gas density and total mass density profiles based on X-ray measurements out to R_{500} for 10 relaxed clusters; all results are derived from Chandra X-ray surface brightness observations in the 0.7–2keV energy band. After correcting for temperature profiles (Vikhlinin et al. [2005]) the count rate is converted into the emission integral EI= $\int n_e n_p dV$, where n_p and n_e are proton and electron density in the hot ICM, respectively. The clusters have redshift range $0.02 - 0.23$, temperature range 0.7–9 keV and mass range 0.77–10.74 $\times 10^{14} M_\odot$. For each cluster they fit the gas density profile to R_{500} with what is essentially the beta model at large radii. Table 2.2.1 gives the best-fit values of the β parameter.

In Table 2.2.1, we have omitted the two lowest mass groups. For the remaining

Table 2.1: Properties of Chandra Clusters

Cluster Name	$M_{500}(10^{14}h_0^{-1}M_\odot)$	f_{500}^{gas}	β_{500}
A383	3.06 ± 0.31	0.124 ± 0.007	0.69 ± 0.02
A133	3.17 ± 0.38	0.083 ± 0.006	0.82 ± 0.04
A907	4.56 ± 0.37	0.124 ± 0.006	0.72 ± 0.02
A1795	6.03 ± 0.52	0.104 ± 0.006	0.87 ± 0.03
A1413	7.57 ± 0.76	0.107 ± 0.007	0.81 ± 0.03
A478	7.68 ± 1.01	0.120 ± 0.011	0.76 ± 0.02
A2029	8.01 ± 0.74	0.123 ± 0.007	0.76 ± 0.03
A2390	10.74 ± 1.08	0.141 ± 0.009	0.70 ± 0.01

Chandra measurements of mass M_{500}, gas fraction f_{500}^{gas} and gas density slope parameter β for 10 relaxed nearby clusters (Vikhlinin et al. [2006]).

groups, the values of β and f^{gas} at R_{500} are quite self-similar. A weighted mean $\overline{\beta}$ of the eight clusters is:

$$\overline{\beta} = \frac{\sum_{i=1}^{N}(\beta_i/\Delta_i^2)}{\sum_{i=1}^{N}(1/\Delta_i^2)} \tag{2.4}$$

where the subscript i refers to the ith cluster and where N equals 8 in this case. To find the error on the mean, we use the formula for standard deviation divided by $\sqrt{N-1}$:

$$\Delta(\overline{\beta}) = \frac{\sqrt{\sum_{i=1}^{N}(\beta_i - \overline{\beta})^2}}{N-1} \tag{2.5}$$

We find $\overline{\beta} = 0.729 \pm 0.016$. Multiplying by 3, the mean gas density slope for the eight clusters is $\overline{\alpha}_{gas} = 2.19 \pm 0.05$. At R_{500}, the NFW total mass density slope is $\alpha_m = 2.57$, considerably steeper than the gas density profile. This is true not only for the mean value of α_{gas} but for all individual clusters, with the result that f^{gas} is a rising function of radius in all cases at the largest radius observed.

X-ray temperatures of the intracluster gas have also been measured via Chandra to greater resolution than ever before (Vikhlinin et al. [2005]). The temperature profiles are also observed to follow an inverse power law with radius. Using both temperature and gas density profiles, and assuming hydrostatic equilibrium, Vikhlinin et al. [2006] derive total mass M_{500} within R_{500}.

$$M_{tot}(r) = -3.68 \times 10^{13} M_{\odot} T(r) r \left(\frac{d \log \rho_g}{d \log r} + \frac{d \log T}{d \log r} \right) \tag{2.6}$$

where T in in units of keV and r is in units of Mpc. Given $M_{tot}(r)$ they determine the gas fraction $f^{gas}(r) \equiv M_{gas}(< r)/M_{tot}(< r)$.

Ettori and Balestra [2009] have selected 11 massive clusters from Chandra data for which it was possible to survey X-ray surface brightness to $\approx R_{200}$. The clusters are hot ($T > 3$keV) and high-redshift ($0.3 < z < 1.3$). Two of these clusters overlap with Vikhlinin et al. [2006]'s sample. They fit a single power-law function to the surface brightness profiles in different radii ranges. The surface brightness is a function of gas density as well as temperature, both of which are power laws: $S_b \propto \int n_{gas}^2 \Lambda(T) dl$ where the integral is along the line of sight. When corrected for the weak dependence of the cooling function on gas temperature in the considered energy band, the surface brightness power-law implies a slope in the gas density profile of $\alpha_{gas} = 2.39 \pm 0.35$ at R_{500}, and $\alpha_{gas} = 2.62 \pm 0.43$ at R_{200}. This suggests a steepening of gas density slope of about 10% from R_{500} to R_{200}, but with a large error bar, such that no steepening with radius is also consistent with Ettori and Balestra [2009]'s results within 1σ. Ettori and Balestra [2009]'s slopes are steeper than other measurements (including Vikhlinin et al. [2006] above), but within their error bars they are consistent.

Sun et al. [2009] present an analysis of 43 galaxy groups and poor clusters ($M_{500} = 10^{13} - 10^{14} M_{\odot}$) at low redshift ($z = 0.012 - 0.12$), based on Chandra archival data, for the purpose of comparison with rich Chandra clusters analyzed by Vikhlinin et al. [2006]. Like Vikhlinin et al. [2006], surface brightness data is collected in the 0.7–2keV energy band, and the surface brightness is fitted to a model which follows the beta model at large radii. After robust background subtraction and modeling, for 11 groups, gas properties can be derived to R_{500}. For an additional 12 groups, gas properties can be derived to at least R_{1000} and properties at R_{500} are estimated from extrapolation. (Three of these, however, are below our minimum threshold mass for groups of $M_{500} = 3 \times 10^{13} M_{\odot}$. So we discard them.) Sun et al. [2009] found the gas fraction to be an increasing function of radius in all cases to R_{500}, indicating that the gas density profile is shallower than the NFW profile for all groups in the sample. Table 2.2.1 gives the mass and gas fraction for each of the 20 groups for which surface brightness could be observed to R_{500}.

2.2.2 XMM-Newton Measurements

Arnaud et al. [2007] and **Pratt et al. [2006]** observe 10 relaxed clusters with XMM-Newton to R_{500} in the band $0.3 - 3.$ keV. The clusters are nearby ($z < 0.2$) with temperatures ranging from 2–9keV. Pratt et al. [2006] (in Appendix A) derive gas density profiles from the emissivity corrected surface brightness profiles using the deprojection and PSF-convolution technique developed by Croston et al. [2006]. They fit the gas density profiles to beta-models. The best-fit values of β are given in Table 2.2.2. Integrating the gas density profile gives total gas mass.

Pointecouteau et al. [2005] derive the mass profile for each cluster from the best fitting gas density profile and the deprojected, PSF-corrected temperature profile

Table 2.2: Properties of Chandra groups

Group	$M_{500}(10^{13}M_{\odot})$	f_{500}^{gas}
MKW4	$4.85^{+0.71}_{-0.68}$	$0.086^{+0.009}_{-0.009}$
3C 442A	$3.90^{+0.22}_{-0.40}$	$0.068^{+0.006}_{-0.003}$
NGC 4104	$4.85^{+0.55}_{-0.53}$	$0.069^{+0.009}_{-0.006}$
A1177	$5.28^{+0.84}_{-0.73}$	$0.060^{+0.009}_{-0.007}$
NGC 6269	$8.49^{+1.97}_{-2.01}$	$0.076^{+0.011}_{-0.010}$
ESO 306-017	$10.3^{+2.1}_{-1.3}$	$0.081^{+0.010}_{-0.011}$
A160	$7.90^{+1.06}_{-1.10}$	$0.085^{+0.009}_{-0.008}$
UGC 842	$5.60^{+2.60}_{-1.10}$	$0.056^{+0.012}_{-0.014}$
A2717	$12.9^{+2.7}_{-1.7}$	$0.076^{+0.010}_{-0.010}$
RXJ 1022+3830	$8.00^{+1.31}_{-1.40}$	$0.075^{+0.007}_{-0.013}$
AS1101	$14.1^{+5.0}_{-3.4}$	$0.114^{+0.021}_{-0.020}$
ESO 351-021	$3.22^{+1.80}_{-0.90}$	$0.074^{+0.013}_{-0.018}$
A3880	$14.9^{+5.0}_{-3.5}$	$0.088^{+0.016}_{-0.021}$
A1991	$13.4^{+2.5}_{-1.9}$	$0.094^{+0.018}_{-0.031}$
A1275	$6.90^{+3.00}_{-1.67}$	$0.094^{+0.012}_{-0.018}$
A2092	$8.95^{+1.81}_{-1.62}$	$0.078^{+0.013}_{-0.013}$
A2462	$8.80^{+1.29}_{-1.19}$	$0.099^{+0.011}_{-0.009}$
RXJ 1159	$8.30^{+3.10}_{-1.12}$	$0.065^{+0.007}_{-0.012}$
A1692	$9.70^{+2.99}_{-1.91}$	$0.090^{+0.014}_{-0.020}$
A2550	$7.90^{+2.90}_{-1.00}$	$0.093^{+0.011}_{-0.016}$

Mass M_{500} and gas fraction f_{500}^{gas} of 20 groups and poor clusters (Sun et al. [2009]).

Table 2.3: Cluster Properties from XMM-Newton Observations

Cluster Name	$M_{500}(10^{14}h_0^{-1}M_\odot)$	f_{500}^{gas}	β_{500}
A2717	$1.10^{+0.13}_{-0.11}$	$0.093^{+0.012}_{-0.011}$	0.63
A1991	$1.20^{+0.13}_{-0.12}$	$0.104^{+0.012}_{-0.011}$	0.65
A2597	$2.22^{+0.23}_{-0.21}$	$0.113^{+0.012}_{-0.013}$	0.73
A1068	$3.87^{+0.29}_{-0.27}$	$0.097^{+0.008}_{-0.007}$	1.01
A1413	$4.82^{+0.44}_{-0.40}$	$0.157^{+0.016}_{-0.014}$	0.71
A478	$7.57^{+1.20}_{-1.02}$	$0.123^{+0.020}_{-0.017}$	0.84
PKS0745-191	$7.27^{+0.80}_{-0.70}$	$0.147^{+0.018}_{-0.016}$	0.64
A2204	$8.39^{+0.86}_{-0.77}$	$0.126^{+0.014}_{-0.012}$	0.91

Mass M_{500}, gas fraction f_{500}^{gas} and the gas density slope parameter β from XMM-Newton observations by Arnaud et al. [2007], Pratt et al. [2006], Pointecouteau et al. [2005]. M_{500} is found from assumptions of hydrostatic equilibrium and NFW mass distribution. Gas density profile is found from fitting to the beta model.

under the assumption of hydrostatic equilibrium (Equation 2.6). They find M_{500} values from fitting mass profiles to NFW models, except for the two lowest mass clusters. Knowing mass of gas and total mass, f_{500}^{gas} can be found. The two smallest clusters could not be observed to R_{500}; for this reason, we discard them. The combined XMM-Newton data from Arnaud et al. [2007], Pointecouteau et al. [2005] and Pratt et al. [2006] for XMM-Newton clusters is given in Table 2.2.2.

Pratt et al. [2006] do not provide error bars on their values of β. Therefore we will not use their values of β to calculate our final average value of β at R_{500}. However, a straight average of Pratt et al.'s β values gives $\overline{\beta} \approx 0.77$ which corresponds to a gas density slope of ≈ -2.3, in good agreement with Vikhlinin et al. [2006].

2.2.3 Sunyaev-Zel'dovich Measurements

Plagge et al. [2009] present Sunyaev-Zel'dovich data of 15 massive X-ray selected clusters measured with the South Pole Telescope at 150 GHz and 220 GHz. Sunyaev-Zel'dovich decrements are observed for all clusters to large radii of R_{200} and R_{vir}. Radial profiles are obtained using a technique that takes into account the effects of the beams and filtering. However, the Sunyaev-Zel'dovich effect measures *pressure*, which is proportional to the ICM density times temperature. In order to obtain accurate density profiles, the Sunyaev-Zel'dovich pressure measurements must be corrected for the temperature profile and then fit with a beta model.

The Sunyaev-Zel'dovich (SZ) effect is produced by the distortion of cosmic microwave background (CMB) photons by collisions with high-energy electrons in the ICM. This effect can be approximated as the sum of two components (Birkinshaw [1999] and references therein): that caused by the random thermal motion of the hot scattering electrons, and that caused by the cluster peculiar velocity relative to the Hubble flow. The former, known as the thermal SZ effect, leads to a distortion of the CMB Planck spectrum of the form

$$f(x) = \left(x \frac{e^x + 1}{e^x - 1} - 4 \right) (1 + \delta_{SZ}(x, T_e)) \tag{2.7}$$

where $x \equiv h\nu / k_B T_{CMB}$ is the dimensionless frequency, T_{CMB} is the temperature of the CMB, T_e is the temperature of the ICM electrons, and δ_{SZ} is a relativistic correction (Itoh et al. [2000]). For nonrelativistic electrons, the distortion results in a decrement in the measured CMB temperature at frequencies below ~ 217 GHz and an increment above. The amplitude of the effect, expressed as a change in temperature ΔT relative to the CMB temperature, is given by

$$\frac{\Delta T}{T_{CMB}} = f(x) y = f(x) \int \sigma_T n_e \frac{k_B T_e}{m_e c^2} dl \tag{2.8}$$

where y is the Compton-y parameter, a measure of integrated pressure as mentioned above. σ_T is the Thomson cross-section, n_e and T_e are the electron number density and temperature in the ICM, respectively, and the integral is along the line of sight. The integrated y-parameter is a quantity proportional to the total thermal energy of the cluster at a given radius, and therefore provides an estimate of the cluster mass. For typical massive clusters, the kinetic SZ effect produces a signal much smaller than the thermal SZ effect, except at frequencies near the ~ 217 GHz thermal SZ null.

In much of the past work on the thermal SZ effect, isothermality was assumed, i.e., temperature was taken to be constant at all radii, and thus the y-profile was simply fitted directly to a beta model in order to estimate gas density profile (e.g., Grego et al. [2000], Reese et al. [2002], Benson et al. [2004], Halverson et al. [2009]). However, observations have shown that the assumption of isothermality is far from valid. Temperature clearly falls with radius, and this must be subtracted from the SZ pressure profile in order to obtain the gas density profile.

Attempts have been made to develop a standard temperature 'correction factor' to convert from SZ pressure profile to gas density profile. For this purpose, a 'universal temperature profile' is needed. There is observational evidence that one exists (Vikhlinin et al. [2005], Sun et al. [2009], etc.). Reiprich et al. [2009], George et al. [2009], Bautz et al. [2009], Hoshino et al. [2010] measure cluster temperature profiles from Suzaku all the way to R_{200} and beyond. They find an inverse power law relationship of temperature with radius, $T(r) \propto r^{-\alpha_T}$, where $\alpha_T \approx 1$. Generally, from $\sim 0.5R_{200}$ to R_{200}, they find a temperature drop of about a factor of two.

Hallman et al. [2007] use nearly 500 cluster simulations to analyze the discrepancy between isothermal-beta SZ profiles, X-ray profiles and the actual gas density profiles. They find a 'universal temperature profile' as above with $\alpha_T = 1.0$, shown by their simulations and confirmed by observations. For the gas density they find a slope of $\alpha_{gas} = 2.4$, or $\beta = 0.8$. Table 2.2.3 (reproduced from Hallman et al. [2007]) gives for

Table 2.4: Beta-model Fits to Simulated X-Ray and Isothermal S-Z Profiles

Method	Median β	$\beta + 1\sigma$	$\beta - 1\sigma$
Isothermal X-ray	0.84	1.02	0.70
Isothermal SZ	1.05	1.27	0.88
X-ray with UTP	0.81	0.97	0.67
SZ with UTP	0.82	0.97	0.69
Actual gas density	0.8	0.8	0.8

Results from Hallman et al. [2007]'s simulations to find a temperature 'correction factor' to convert from an isothermal beta model fit to SZ decrements, to the actual gas density profile. SZ decrements give a combined measure of gas density times temperature. The table shows the β-parameters obtained from fitting a beta model directly to SZ and X-ray measurements, and the beta-parameters obtained after correcting both for a universal temperature profile (UTP) (see text).

R_{200} the β-parameters obtained from fitting a beta model directly to isothermal SZ and X-ray measurements, and the β-parameters obtained after correcting both for a universal temperature profile (UTP) as stated above. As can be seen from the results, an isothermal beta-fit to the SZ profile yields $\beta = 1.05$, which is different than the 'true' gas density $\beta = 0.8$ (a parameter set in the simulations) by a factor of 1.3. We use this as the correction factor, with an error bar on the correction factor of roughly 0.1.

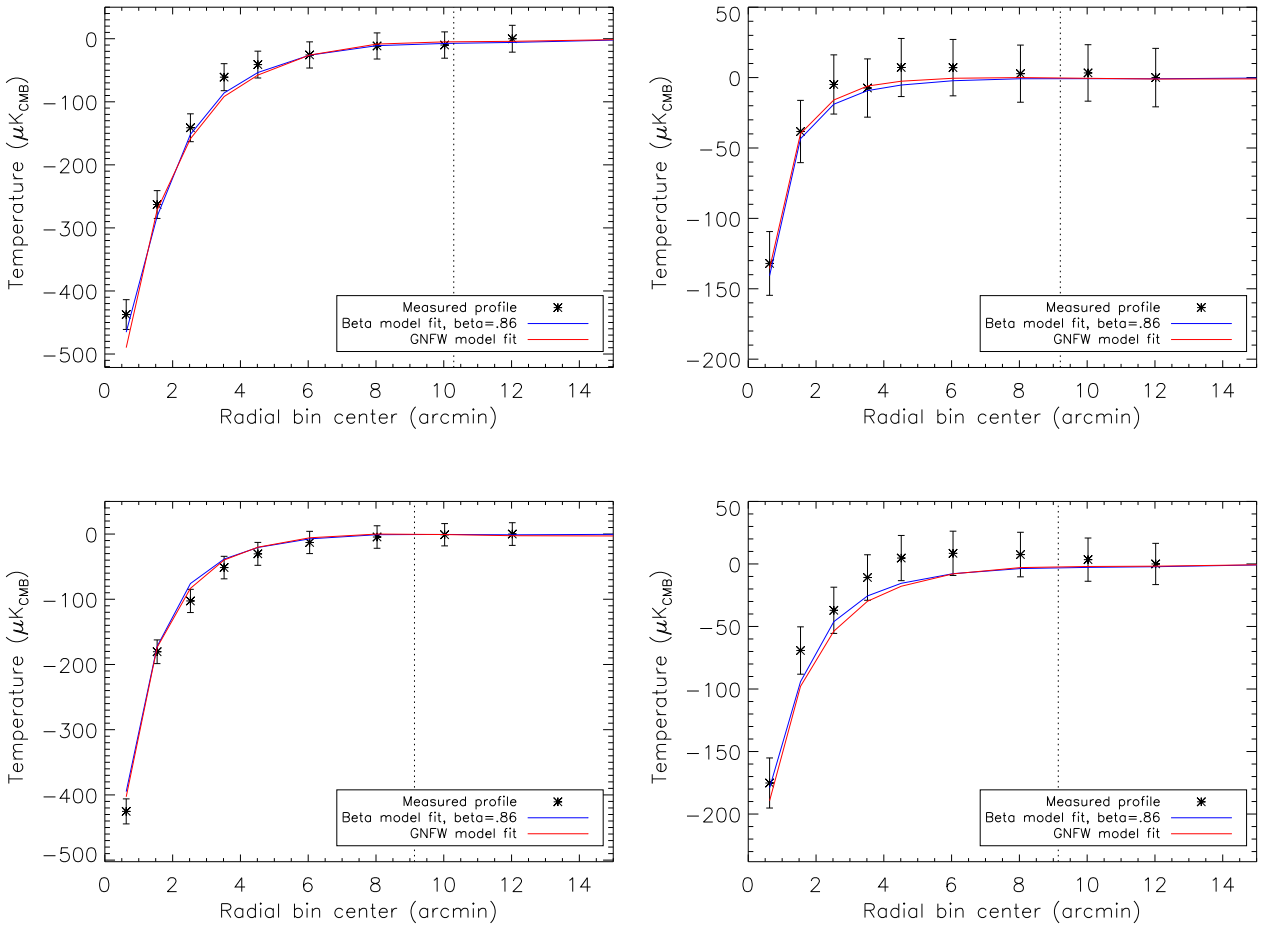

Figure 2.2: Beta-model fits to SZ-decrements of four out of fifteen clusters observed to R_{200} by the South Pole Telescope (Plagge et al. [2009]). The models fit very well to R_{200} and beyond. The vertical dashed lines are estimates of $\sqrt{500/\Delta_c}R_{500}$ where Δ_c is calculated according to Bryan and Norman [1998].

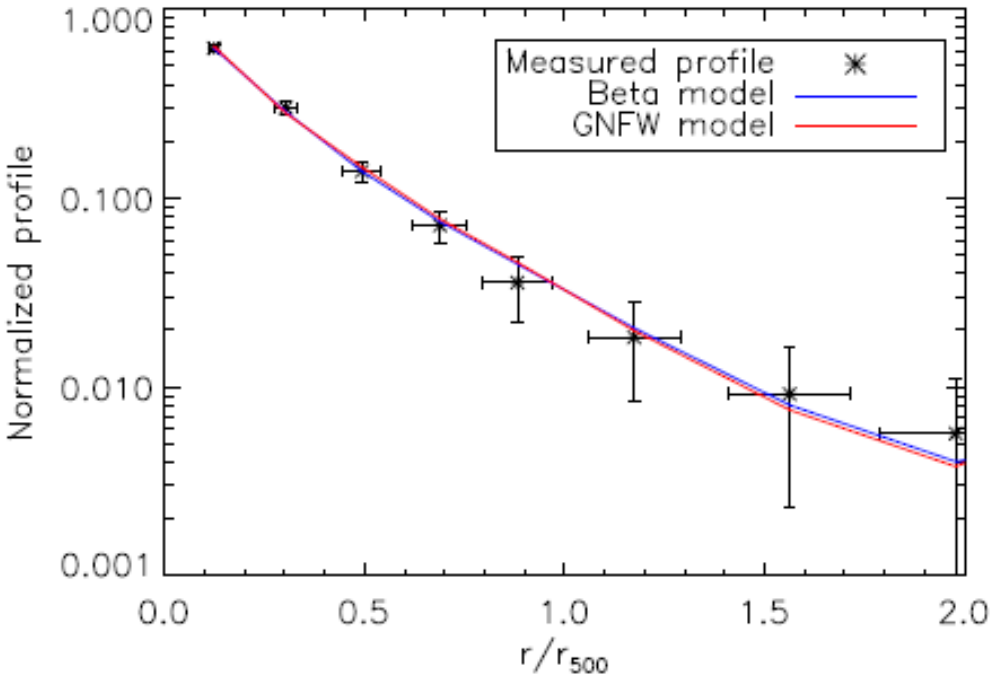

Figure 2.3: Beta-model fit to stacked SZ-decrements of fifteen clusters observed to R_{200} by the South Pole Telescope (Plagge et al. [2009]). The models fit very well to R_{200} and beyond.

Plagge et al. [2009] stack their cluster profiles weighted by noise, scale them to R_{500}, and then fit them with an isothermal β-model. This model provides an excellent fit all the way to R_{vir} (Figure 2.2.3). Their best fit value for β_{SZ} is 0.86 ± 0.09 at R_{500}. (The model fits to beyond R_{500}, but they evaluated β at R_{500} in order to compare with previous work.) Correcting this for a factor of 1.3 ± 0.1 from Hallman et al. [2007], we get $\beta = 0.68 \pm 0.09$, or gas density slope $\alpha_{gas} = 2.03 \pm 0.27$. Since the beta-model fits so well with raw SZ profile, the error in the final β is mostly due to uncertainty in the correction factor.

Umetsu et al. [2009] use SZ measurements from AMiBA, and mass profiles

Table 2.5: Cluster Properties from SZ Measurements with AMiBA

Cluster	$M_{500}(10^{14}M_{\odot})$	f_{500}^{gas}	f_{200}^{gas}
A1689	$11.5^{+0.13}_{-0.12}$	$0.115^{+0.029}_{-0.029}$	$0.119^{+0.031}_{-0.030}$
A2142	$7.9^{+0.22}_{-0.16}$	$0.169^{+0.046}_{-0.034}$	$0.183^{+0.049}_{-0.037}$
A2261	$9.3^{+0.17}_{-0.16}$	$0.103^{+0.036}_{-0.033}$	$0.108^{+0.040}_{-0.035}$
A2390	$6.7^{+0.15}_{-0.14}$	$0.153^{+0.075}_{-0.049}$	$0.164^{+0.084}_{-0.053}$

M_{500} measured from Subaru weak lensing, and f^{gas} determined from AMiBA SZ profile combined with X-ray temperatures, for four massive clusters (Umetsu et al. [2009]). f^{gas} increases in all cases from R_{500} to R_{200}. f_{500}^{gas} is in very good agreement with Chandra and XMM clusters (Vikhlinin et al. [2006], Arnaud et al. [2007]).

from weak lensing with Subaru, to constrain baryon fraction in four clusters. The cluster are massive, with mean $M_{500} \approx 9 \times 10^{14} M_{\odot}$. They correct the SZ-obtained pressure profiles with published X-ray temperatures (Reese et al. [2002], Markevitch et al. [1998], Boehringer et al. [1998], Sanderson et al. [2003]). Thus they constrain f^{gas} at R_{500} and R_{200}, as shown in Table 2.2.3. f^{gas} increases in all cases from R_{500} to R_{200}. f_{500}^{gas} is in very good agreement with Chandra and XMM clusters (Vikhlinin et al. [2006], Arnaud et al. [2007]). Averaging, we get:

$$\overline{f}_{500}^{gas} = 0.126 \pm 0.019 \pm 0.016 \tag{2.9}$$

and

$$\overline{f}_{200}^{gas} = 0.133 \pm 0.020 \pm 0.018, \tag{2.10}$$

where the first error is statistical, and the second is the standard error due to cluster-to-cluster variance.

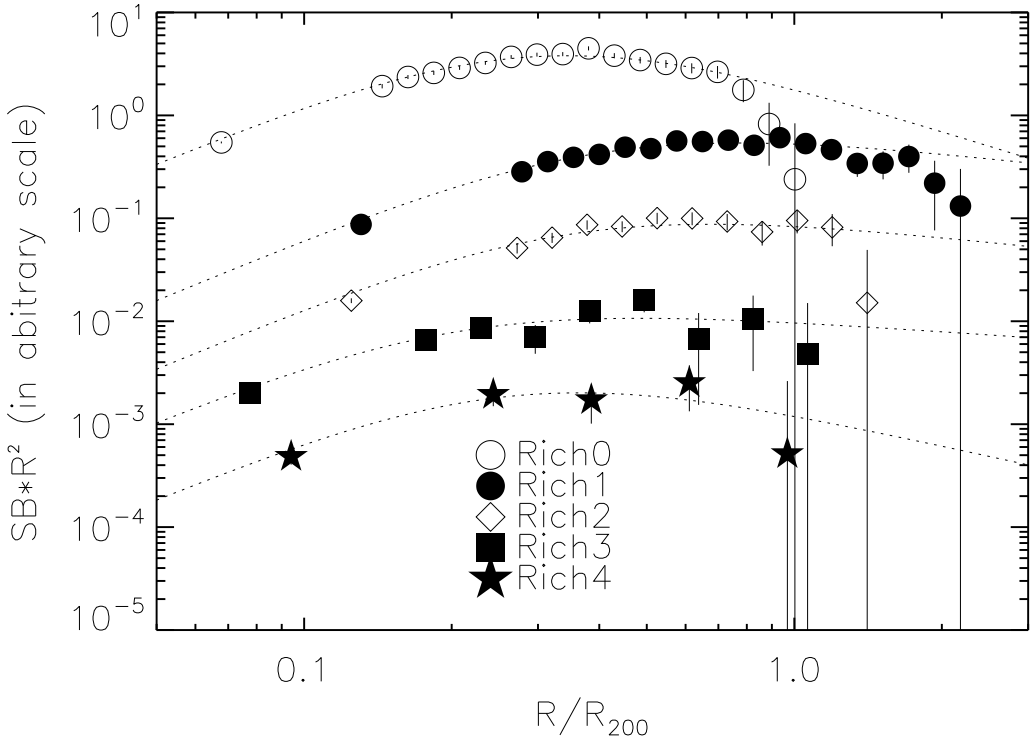

Figure 2.4: Normalized surface brightness profiles of the stacked RASS images of the 2MASS clusters from Dai et al. [2009], multiplied by R^2 and in arbitrary units. Surface brightness is fit with a β-model (shown by dashed lines), $S(R) \propto (1 + (r/R_c)^{(-3\beta+1/2)})$, which corresponds to a three-dimensional gas density profile of $\rho_{gas}(r) \propto (1 + (r/r_c)^{-3\beta/2})$, where $R_c = r_c$. The richest clusters (Class 0, empty circles) show a steep decline beyond R_{200}.

2.2.4 ROSAT Measurements

Dai et al. [2009] observe 2MASS baryon fractions in groups and clusters as a function of cluster richness using total and gas masses from stacked ROSAT X-ray data. For all richness classes they observe to R_{200} or beyond. Their highest richness class 0 corresponds to $M_{500} = 3.2 \pm 0.7 \times 10^{14} M_{\odot}$. For this richness class, they fit a beta model and retrieve $\beta = 0.75 \pm 0.05$, or $\alpha_{gas} = 2.25 \pm 0.15$. For the next next richness class 1 which corresponds to $M_{500} = 0.43 \pm 0.1 \times 10^{14} M_{\odot}$, they fit $\alpha_{gas} = 1.8 \pm 0.18$. At roughly R_{200}, the surface brightness for the richness class 0 drops steeply below the beta model profile. Richness class 1 shows no such decline. This steep decline in gas density profile for the richest clusters beyond R_{200} is a matter of concern, as our analysis will assume smooth extrapolation of the gas density profile to the virial radius. Indeed, for their richness class 0, f^{gas} shows no change from R_{500} to R_{200}, implying that the gas density profile steepens to follow the NFW profile in this radial range. For richness class 1, f^{gas} shows a significant rise to R_{200}. Nevertheless, even for richness class 0, their slope is valid to R_{200} and contributes to the calculation of the value of α_{gas} at R_{500}, or our 'baseline'.

2.2.5 Suzaku Measurements

Suzaku observations are remarkable because they go out to R_{200} or beyond, albeit with low resolution. **Bautz et al. [2009]** report Suzaku observations of the cluster Abell 1795 ($kT \approx 5.3$ keV) extending all the way to $R_{200} = 1.9$ Mpc. Their deprojected gas density profile approaches a power law at large radius, with $\alpha_{gas} = 2.27 \pm 0.07$ at R_{500}. They also observe that $T(r) \propto r^{-0.9}$. This allows them to invoke hydrostatic equilibrium and calculate $M_{500} = 4.1^{+0.5}_{-0.3} \times 10^{14} M_{\odot}$.

George et al. [2009] measure X-ray emission from the PKS 0745-191 ($z = 0.1$,

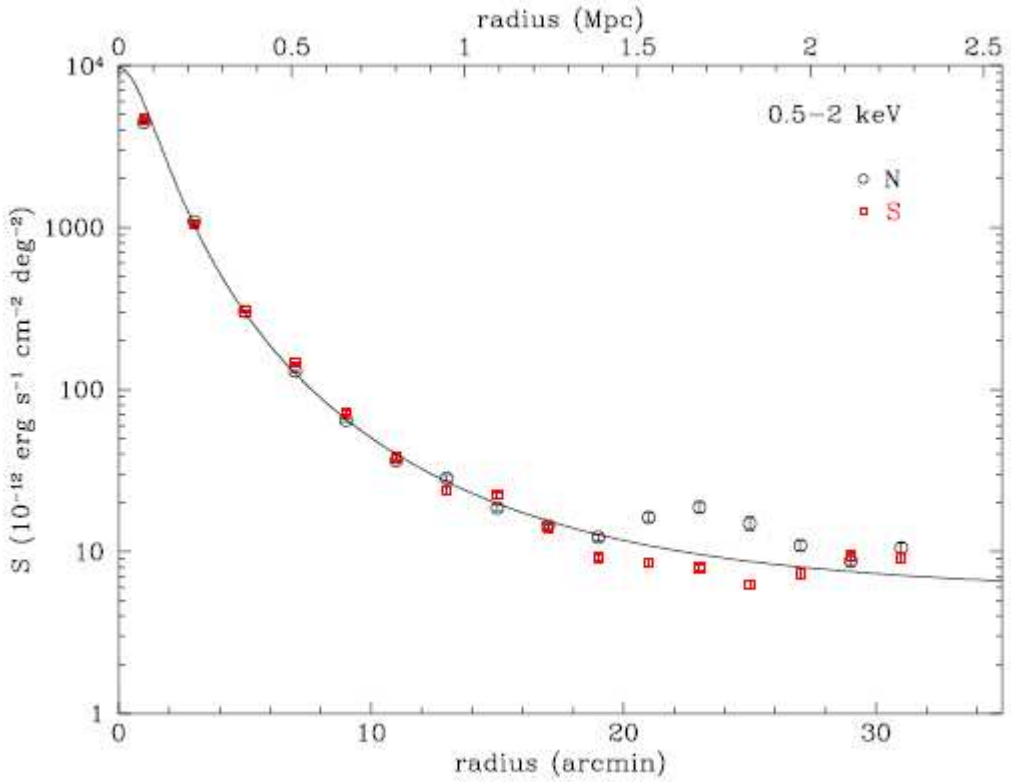

Figure 2.5: Surface brightness profile for Abell 1795 using Suzaku X-ray data (Bautz et al. [2009]), northward (black circles) and southward (red circles) from the cluster center in the 2–8 keV band. The solid curve shows the best-fit β-model fit to all the points.

$M_{200} = 6.4 \pm 0.6 \times 10^{14} M_{\odot}$) all the way to R_{100}. Using the temperature profile and hydrostatic equilibrium, they fit an NFW profile to total mass and a power law to gas density. Oddly enough, their data points for n_H and r (personal correspondence) show the density profile growing shallower (rather than steeper) at large radii. The best fit to R_{100} is $\alpha_{gas} = 2.10 \pm 0.01$. Not considering the central region ($\approx 0.5 R_{500}$) yields an even shallower result, $\alpha_{gas} \sim 1.7$. However, the authors report based on the same data $\alpha_{gas} = 2.23 \pm 0.01$. These calculations are far more than 1 σ apart from one another (possibly due to underestimated error bars in this paper), which makes the results dubious. We can only conclude that the gas density slope in PKS 0745-191 is $\alpha_{gas} \approx 2 \pm 0.3$ at large radii.

Table 2.6: Summary of Observations of the Gas Density Slope at R_{500} and R_{200}

Source	Data	Radius	α_{gas}
Vikhlinin et al. (2006)	10 Chandra clusters	R_{500}	2.19 ± 0.05
Plagge et al. (2009)	SZ measurements of 15 SPT clusters	R_{200}	2.03 ± 0.27
Ettori et al. (2009)	11 Chandra clusters	R_{500}	2.39 ± 0.35
		R_{200}	2.62 ± 0.43
Bautz et al. (2009)	Abell 1795 by Suzaku	R_{500}	2.27 ± 0.07
Dai et al. (2010)	richest 2MASS clusters	R_{200}	2.25 ± 0.15

2.2.6 Summary: Gas Density Slope at R_{500} and Beyond

Table 2.2.6 summarizes the observed gas density slope $\alpha_{gas} = d\log\rho_{gas}/d\log r$ at R_{500} and/or R_{200} from various observations listed above. We use R_{500} as our 'baseline' for extrapolation, as we have sufficient observational data to precisely constrain α_{gas} as well as f^{gas} at R_{500}.

Using these observations we find the mean value of gas density slope at R_{500} using a weighted mean:

$$\overline{\alpha}_{gas} = \frac{\sum_{i=1}^{N}(\alpha_{gas,i}/\Delta_i^2)}{\sum_{i=1}^{N}(1/\Delta_i^2)} \tag{2.11}$$

where i refers to the ith source. To find the error on the mean, we used the formula for the standard deviation divided by $\sqrt{N-1}$, where N is the number of contributing sources.

$$\Delta(\overline{\alpha}_{gas}) = \frac{\sqrt{\sum_{i=1}^{N}(\alpha_{gas,i} - \overline{\alpha}_{gas})^2}}{N-1} \tag{2.12}$$

This comes out to be

$$\overline{\alpha}_{gas} = \mathbf{-2.21 \pm 0.05} \tag{2.13}$$

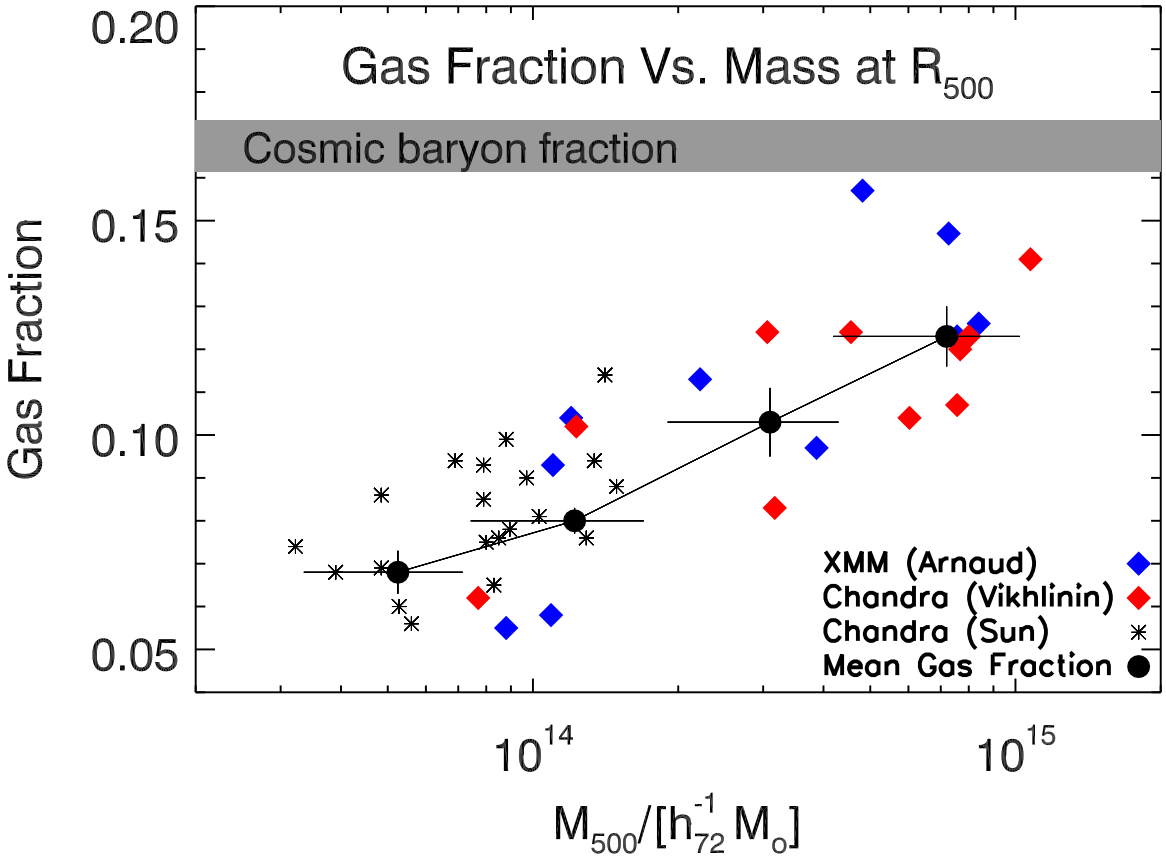

Figure 2.6: Cluster gas fraction as a function of total mass at R_{500}. The clusters are observed with Chandra and XMM-Newton (Vikhlinin et al. [2006], Arnaud et al. [2007], Sun et al. [2009]).

at R_{500}. This is significantly shallower than the NFW dark matter slope at R_{500} of $\alpha_m = 2.57$. If the gas density slope continues to be flatter than the NFW slope beyond R_{500}, the gas fraction will increase with radius beyond R_{500}.

2.3 The Stellar Fraction

Stars constitute approximately 10–40% of baryons, or 2–4% of total mass in groups and clusters. Stellar fraction has been observed to have a correlation with mass: it seems to be higher in groups and poor clusters than in rich clusters (e.g., Giodini et al. [2009], Lin et al. [2003], Gonzalez et al. [2005]; Bryan [2000]). **Lin et al. [2003]** analyzed near-infrared data for 13 clusters selected from the 2MASS survey. The mass range is $M_{500} = 10^{14} - 10^{15} M_{\odot}$. For each cluster they multiplied the total K-band luminosity by the average stellar mass-to-light ratio ($\overline{\Upsilon}_{star}(T_X)$) for that cluster. The mean stellar mass-to-light ratio was estimated from observations of elliptical and stellar galaxies (Gerhard et al. [2001]; Bell and de Jong [2001]), after taking into account the varying spiral fraction as a function of temperature (Bahcall [1977]; Dressler [1980]). To find M_{500}, they use an X-ray $M - T_X$ relation obtained by Finoguenov et al. [2001] from ASCA profiles. They find the following correlation between stellar fraction and M_{500}:

$$f_{500}^{stars} \equiv \frac{M_{star}}{M_{500}} = 1.64^{+0.10}_{-0.09} \times 10^{-2} \left(\frac{M_{500}}{3 \times 10^{14} M_{\odot}} \right)^{-0.26 \pm 0.09} \tag{2.14}$$

Giodini et al. [2009] investigate the behavior of stellar fraction with mass for a bigger mass range than Lin et al. [2003], $M_{500} = 10^{13} - 10^{15} M_{\odot}$. For this purpose, they complement the 2MASS sample of Lin et al. [2003] with 91 low mass groups ($M_{500} = 10^{13} - 10^{14} M_{\odot}$) from the COSMOS Survey. They determine total mass for the COSMOS sample from weak lensing, which is more robust than the scaling

relation used by Lin et al. [2003]. They improve the mass estimates of Lin et al. [2003] by applying instead the more recent scaling relations by Pratt et al. [2006]. They find total stellar mass from K-band luminosity in a manner similar to Lin et al. [2003]'s.

For the COSMOS groups alone, Giodini et al. [2009] find the following scaling relation of stellar fraction with halo mass:

$$f_{500}^{stars} = 5.0^{+0.1}_{-0.1} \times 10^{-2} \left(\frac{M_{500}}{5 \times 10^{13} M_{\odot}} \right)^{-0.26 \pm 0.09} \tag{2.15}$$

However, looking at Figure 2.7, we note that either sample taken by itself displays a weaker trend with mass than the combined sample. The open squares (2MASS clusters) by themselves show a weak, shallow trend. The filled grey circles (COSMOS groups) on their own show a similarly weak trend. Taken together, the combined sample shows a strong trend (solid line). We also note that the two samples are holistically slightly displaced vertically on the plot, perhaps due to the different techniques of mass determination used by each author. The trend could reflect the discrepancy in mass calibration, as well as a true variation in stellar fraction. If this is the case then the stellar fraction could be a slightly shallower function of mass, closer to $M^{-0.3}$ as found by each sample individually. This does not make a big difference to our baryon fraction. However, there is considerable overlap between the two samples and they seem to be continuous. So the concerns could be ill-founded. In any case, taking one sample at a time is not a viable option because the mass range of each individual sample is too small to yield a robust scaling relation with mass.

So we adopt the scaling relation displayed by the combined sample (solid line in Figure 2.7):

$$f_{500}^{stars} = 5.0^{+0.1}_{-0.1} \times 10^{-2} \left(\frac{M_{500}}{5 \times 10^{13} M_{\odot}} \right)^{-0.37 \pm 0.04} \tag{2.16}$$

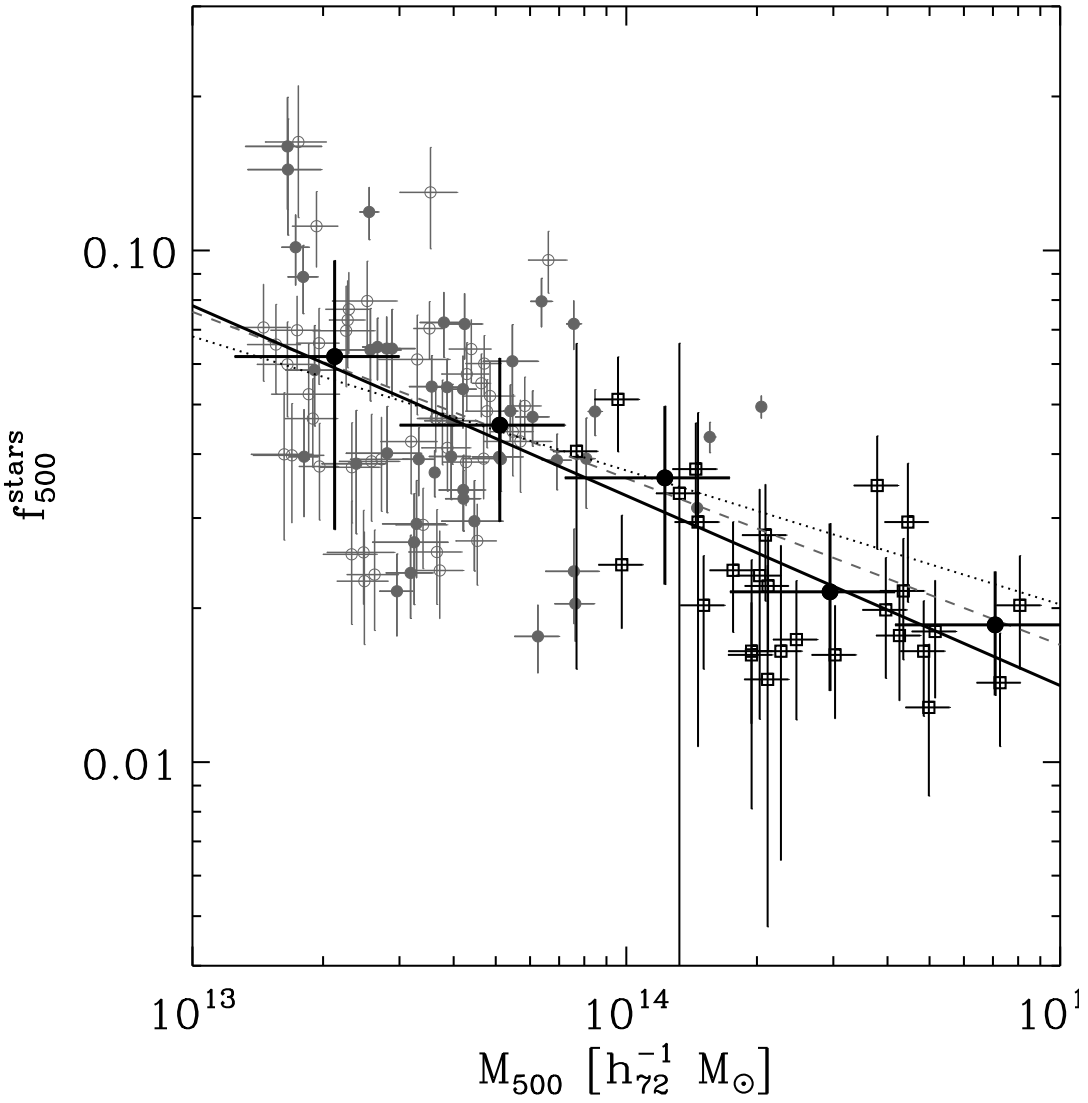

Figure 2.7: Stellar-to-total mass ratio vs. total mass, for the combined sample of 91 COSMOS groups (grey circles) and 27 2MASS clusters (empty squares) (Giodini et al. [2009], Lin et al. [2003]). The solid line shows the best fit relation for the combined sample. The dashed and dotted lines show fits to COSMOS clusters only. The large points show the bi-weight mean and standard deviation for the combined data binned into five logarithmic bins by mass. (Source: Giodini et al. [2009])

Thus, stars contribute roughly 40% to the baryon content in low mass clusters ($< 10^{14} M_{\odot}$) but only about 13% in high-mass clusters. This implies a strong downward trend in star-formation efficiency from groups to clusters. The underlying cause (Springel and Hernquist [2003]) might be the less efficient formation of cooling flows in halos with virial temperatures above 10^7 K.

The stellar fraction is higher near the core than at the outskirts of the cluster, but at the radial range of $R_{500} - R_{vir}$ that we are interested in, the stellar fraction is expected to remain constant to a good approximation.

Gonzalez et al. [2007] have also investigated stellar fraction in groups and clusters. Their stellar fraction-mass relation is considerably steeper than that of either Lin et al. [2003] or Giodini et al. [2009]. Their sample is biased towards systems with dominant brightest cluster galaxies (BCG), which might artificially boost the mean stellar fraction in their sample.

2.4 Diffuse Intracluster Light (ICL)

The last piece we need in order to account for baryons in clusters is intracluster stars stars, which emit diffuse intracluster light in the near-infrared part of the spectrum. The unambiguous detection of intracluster light (ICL) in nearby clusters was made possible by the advent of high-sensitivity panoramic CCD detectors which measured at very faint surface brightness levels, from ~ 26 down to ~ 30 mag$_R$ arcsec^{-2} (Bernstein et al. [1995], Gonzalez et al. [2000], Gonzalez et al. [2005], Feldmeier et al. [2002], Feldmeier et al. [2004]). It is worth noting that the dynamical definition of ICL we gave above cannot apply to photometric measurements (Zibetti [2008]). All photometric studies of the ICL have to *define* criteria, like surface brightness thresholds and/or profile decompositions, to isolate the ICL from the rest of the optical cluster light, in a way that does not need to be consistent with dynamical definitions.

Zibetti [2008] used stacking analysis of 683 clusters at $z = 0.2$–0.3 ranging in total mass from a few times 10^{13} to $5 \times 10^{14} M_{\odot}$ (the average total mass is $7 \times 10^{13} M_{\odot}$), selected from a 1500 deg^2 of SDSS-DR1, reaching the unprecedented surface brightness limit of $\sim$32 mag arcsec^2 (R band in the $z = 0.25$ observed frame). They show that on average the ICL contributes a constant 11%–22% of the stellar light within 500 kpc. In a complementary study, Krick and Bernstein [2007] used a sample of massive clusters with a range of morphology, redshift and densities to find that the ICL contributes 6%–22% to the total cluster light in the R band within one quarter of the virial radius, finding no appreciable correlation with cluster mass.

Given these results, one concludes that the contribution of the ICL to the total mass of a system ranges between 11% and 22%. This range is consistent with the theoretical results by Murante et al. [2007] and Purcell et al. [2008] in their attempt at modeling the ICL by numerical simulations. In this paper, we assume a lower value of 10% for ICL contribution to total stellar fraction, in order to get a conservative estimate of total baryon fraction. Under this assumption, we can rewrite the stellar fraction relation versus mass (Equation 2.3) to include an additional 10% contribution of ICL:

$$f_{500}^{stars} = 5.5^{+0.1}_{-0.1} \times 10^{-2} \left(\frac{M_{500}}{5 \times 10^{13} M_{\odot}} \right)^{-0.37 \pm 0.04} \tag{2.17}$$

2.5 Putting It All Together: the Baryon Fraction

Using the observed stellar fraction relation in Equation 2.4, the stellar fraction in the clusters and groups observed by our sources, i.e., Vikhlinin et al. [2006], Sun et al. [2009], Arnaud et al. [2007], can be estimated. Recall that for each cluster or group, we know f^{gas} at R_{500}, as given in Tables 2.2.1, 2.2.1, and 2.2.2.

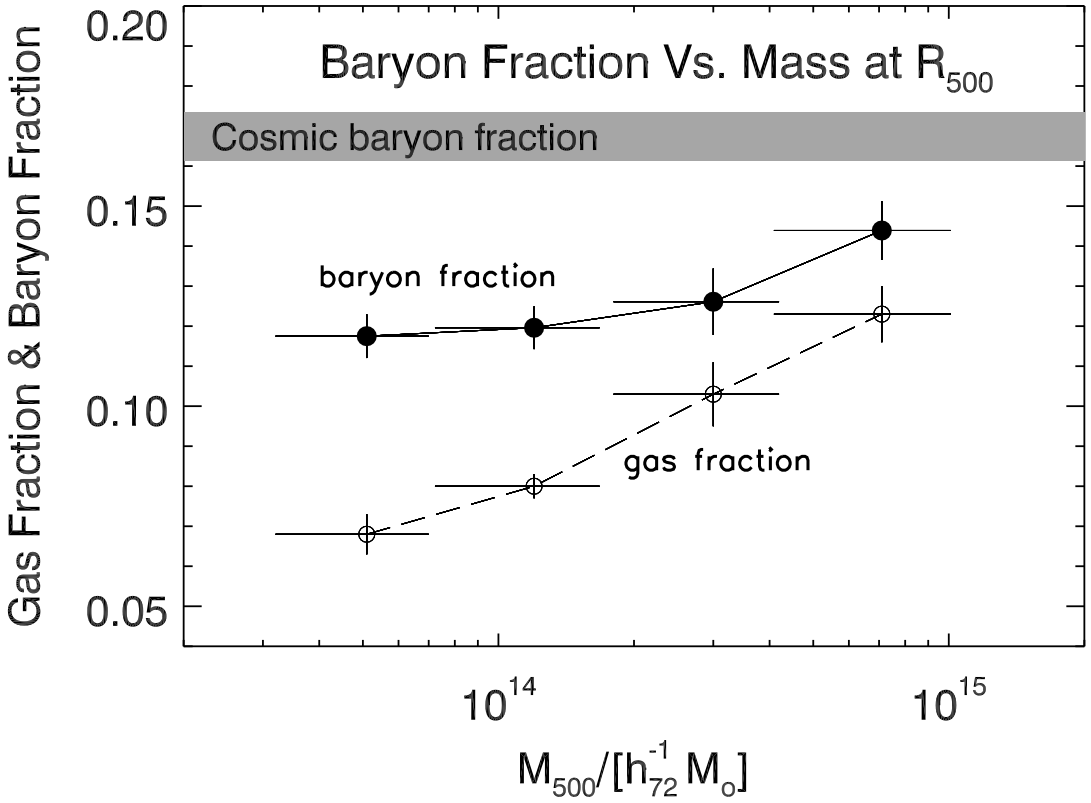

Figure 2.8: Gas and total baryon fractions (including ICL contribution of 11%) for four cluster mass bins at R_{500}. The clusters are taken from Vikhlinin et al. (2006), Arnaud et al. (2007) and Sun et al. (2009).

Table 2.7: Gas, Stellar and Total Mass Fraction at R_{500}

Bin	$M_{500}(/M_\odot)$	f_{500}^{gas}	f_{500}^{stars}	$f_{500}^{stars+gas}$
1	5.1×10^{13}	0.068 ± 0.005	0.049 ± 0.002	0.117 ± 0.028
2	1.2×10^{14}	0.080 ± 0.003	0.039 ± 0.004	0.119 ± 0.005
3	3.0×10^{14}	0.103 ± 0.008	0.023 ± 0.002	0.126 ± 0.009
4	7.1×10^{14}	0.123 ± 0.007	0.021 ± 0.002	0.143 ± 0.007

Gas, stellar and baryon fraction (including ICL) at R_{500} for four logarithmic mass bins (see text). Sources for f_{500}^{gas} are Chandra and XMM observations by Vikhlinin et al. [2006], Arnaud et al. [2007], Sun et al. [2009]. The stellar mass fraction is derived from the scaling relation of Giodini et al. [2009], Lin et al. [2003] and ICL calculations of Zibetti [2008] (Equation 2.4).

We divide the 38 clusters and groups from these sources into four logarithmic bins of equal mass (after Giodini et al. [2009]). The "mean" mass for each bin is simply the logarithmic middle value.

The highest mass bin, Bin 4, which ranges from $4.2\times10^{14}M_\odot$ to $10.0\times10^{14}M_\odot$. has 10 clusters. The second to highest mass bin, Bin 3, which ranges from $1.7\times10^{14}M_\odot$ to $4.2\times10^{14}M_\odot$, has 4 clusters. Bin 2, which ranges from $0.7\times10^{14}M_\odot$ to $1.7\times10^{14}M_\odot$, has 19 poor clusters. And the least massive bin, Bin 4, which ranges from $3.2\times10^{13}M_\odot$ to $7.0\times10^{13}M_\odot$, has 7 poor clusters/groups.

To find the mean f^{gas} for each bin, we calculate a mean (weighted by error) of all the clusters in that bin.

$$\overline{f}^{gas} = \frac{\sum_{i=1}^{N}(f_{gas,i}/\Delta_i^2)}{\sum_{i=1}^{N}(1/\Delta_i^2)} \tag{2.18}$$

where i refers to the ith member of that bin. The error on mass is simply the mass range of each bin. The error bar on each f^{gas} is the error on the mean, i.e., the standard deviation of f_{gas} values in each bin divided by $\sqrt{N-1}$, where N is the number of clusters in the bin.

$$\Delta(\overline{f}^{gas}) = \frac{\sqrt{\sum_{i=1}^{N}(f_{gas,i} - \overline{f}^{gas})^2}}{N-1} \tag{2.19}$$

The error on the total baryon fraction for each bin is derived by adding the errors in the stellar fraction and the gas fraction respectively in quadrature.

$$\Delta(f^{stars+gas}) = \sqrt{\Delta(f^{gas})^2 + \Delta(f^{stars})^2} \tag{2.20}$$

Table 2.5 allows us to derive the following correlation between f_{500}^{gas} and M_{500}.

$$f_{500}^{gas} = (9.3 \pm 0.2) \times 10^{-2} \left(\frac{M_{500}}{2 \times 10^{14} M_{\odot}} \right)^{0.21 \pm 0.03} \tag{2.21}$$

Even though the stellar fraction is a decreasing function of total mass, the gas mass is 5–10 times the stellar mass in our mass range, so that $f^{stars+gas}$ remains an increasing function of mass. The baryon fraction versus total mass relation, as calculated without ICL by Giodini et al. [2009], is:

$$f_{500}^{stars+gas} = (0.123 \pm 0.003) \times \left(\frac{M_{500}}{2 \times 10^{14} M_{\odot}} \right)^{0.09 \pm 0.03} \tag{2.22}$$

Chapter 3

Analysis and Results

The last chapter established observational findings at R_{500} and R_{200} in order to provide us with a framework for extrapolation of baryon fraction to larger radii. In Section 2.1 we established from the NFW profile that the matter density is proportional to $r^{-2.57}$ at R_{500}. In Section 2.2 we established from observations that the gas density profile is proportional to $r^{-2.21\pm0.05}$ at R_{500}, shallower than the NFW profile at the same radius. We also collected observations to find mean gas fraction and stellar fraction for various mass bins of clusters at R_{500}.

In this chapter, we will use these observations to extrapolate the baryon fraction to the virial radius (R_{100}). We assume that the total mass continues to follow the NFW profile up to the virial radius. To extrapolate the gas density profile, we rely on observations that provide gas density slopes to either R_{200} or beyond (Ettori and Balestra [2009], Dai et al. [2009], George et al. [2009] and Plagge et al. [2009]).

Plagge et al. [2009] observed the Sunyaev-Zel'dovich decrements for 15 massive clusters accurately to nearly the virial radius using the South Pole Telescope. They fit the data to a beta model and find an excellent fit up to the virial radii of the clusters. Assuming isothermality, they found isothermal $\beta = 0.86 \pm 0.09$. But since the temperature does not stay constant with radius, a correction for the temperature

profile is needed in order to obtain the gas density profile. We use the results from Hallman et al. [2007]'s simulations to derive a correction factor of 1.3 ± 0.1 (as shown in Section 2.2.3), and thus obtained a density profile from Plagge et al. [2009]'s SZ measurements of $\alpha_{gas} = 2.03 \pm 0.27$ at R_{200}.

Ettori and Balestra [2009] provide a measurement of the trend of α_{gas} to R_{200} from Chandra observations of 11 massive clusters. On average, they observe a steepening of the gas density slope by $\approx 10\%$, from 2.39 ± 0.35 at R_{500} to 2.62 ± 0.43 at R_{200}. At R_{500} their slope is steeper than most other observations (see Section 2.2), though consistent within their large error bars. We normalize Ettori and Balestra [2009]'s gas density slope to our mean observed value, and follow their relative trend to larger radii. Therefore, we take from Ettori and Balestra [2009] the trend of steepening of α_{gas} by 10% from R_{500} to R_{200}. According to this trend, our value of α_{gas} should steepen from 2.21 ± 0.05 at R_{500}, to 2.4 ± 0.05 at R_{200}.

Dai et al. [2009] observe surface brightness profiles of stacked ROSAT clusters to R_{200}. The surface brightness is given by $S = \int \rho_{gas}^2 \Lambda(T) dl$ where the integral is along the line of sight and $\Lambda(T)$ is the cooling function which has a weak dependence on T. For the gas density, they find $\alpha_{gas} = 2.25 \pm 0.15$ which fits well to R_{200}.

Other observations which extend to R_{200} are less reliable. We saw that George et al. [2009] observed the cluster PKS 1745-191 with Suzaku X-ray data. Although George et al. [2009]'s measurements extend to R_{100} and therefore provide valuable information, their quantitative results are fraught with difficulties. The gas density profile in their cluster PKS 0745-191 appears to get shallower (rather than steeper) at large radii, which is at odds with other observations. The spatial resolution of Suzaku is low and the radial mass bins have large error bars, resulting in an uncertain gas density slope. Therefore, we do not use George et al. [2009]'s results in our analysis.

In light of the above observations, we have developed three plausible scenarios for

the gas density profile beyond R_{500}.

1. We use the average of the three observed values of α_{gas} at R_{200} mentioned above: 2.03 ± 0.27 (from Plagge et al. [2009]), 2.4 ± 0.27 (normalized from Ettori and Balestra [2009]), and 2.25 ± 0.15 (from Dai et al. [2009]). The weighted mean is $\approx 2.23 \pm 0.1$ at R_{200}. However, we will keep the error of ± 0.05 on our extrapolated gas density slopes similar to the slope at R_{500}. Therefore, the error bars on the extrapolated gas fraction reflect only the observed uncertainty at the baseline of R_{500}; they do not reflect the uncertainty in the behavior of α_{gas} beyond R_{500}. Since our observed value of α_{gas} at R_{500} is already 2.21 ± 0.05, this scenario amounts to no steepening to R_{200}. We call this the FIXED SLOPE SCENARIO.

2. In this scenario we allow α_{gas} to steepen. We propose that, even though the gas density profile has been observed to be more spread out than the NFW profile, it would be a conservative scenario to assume that the gas density profile falls at the same trend as the NFW profile. The NFW profile steepens by 4% from 2.57 at R_{500} to 2.65 at R_{200}, and then by another 4% to 2.74 at R_{100}. Accordingly, in this scenario, α_{gas} steepens from 2.21 ± 0.05 at R_{500} by 4% to 2.3 ± 0.05 at R_{200} and to 2.4 ± 0.05 at R_{100}. We call this the NFW TREND. We consider this the most realistic scenario.

3. This is the most CONSERVATIVE SCENARIO, in which α_{gas} follows the profile seen in Chandra observations of Ettori and Balestra [2009], which show the most steepening of all the observations. They observe average slope to steepen by 10% from R_{500} to R_{200}. Thus, in this scenario, α_{gas} steepens by 10% from 2.21 ± 0.05 at R_{500}, to 2.4 ± 0.05 at R_{200}. In the next interval from R_{200} to R_{100}, α_{gas} steepens by another 10% to 2.6 ± 0.05 at R_{100}.

The results of FIXED SLOPE SCENARIO, where no steepening in the gas density profile takes place, are shown in Figures 3.1 and 3.2, for R_{200} and R_{vir}. The gas fraction at R_{200} is found from extrapolating the gas fraction from the observed baseline at R_{500}. In general,

$$f^{gas}(r) \equiv \frac{M_{gas}(\leq R)}{M_{tot}(\leq R)} = \frac{\int_0^R \rho_{gas}(r) 4\pi r^2 dr}{\int_0^R \rho(r) 4\pi r^2 dr} \tag{3.1}$$

At large radii, however, the scaling becomes simple:

$$f^{gas}(r) \approx \frac{\rho_{gas}(R)}{\rho(R)} = \frac{r^{-\alpha_{gas}}}{r^{-\alpha_m}} = r^{\alpha_m - \alpha_{gas}} \tag{3.2}$$

Therefore, by this simple scaling relation at large radii, we extrapolate the gas fraction from R_{500} to R_{200}:

$$f^{gas}_{200} = f^{gas}_{500} \left(\frac{R_{200}}{R_{500}} \right)^{\alpha_m - \alpha_{gas}} \tag{3.3}$$

The gas fraction at R_{100} is found similarly by extrapolating from R_{200}. Recall that for the interval between R_{500} and R_{200}, the mean NFW profile slope is $\overline{\alpha_m} = 2.61$. For the interval between R_{200} and R_{100}, the mean NFW profile slope is $\overline{\alpha_m} = 2.70$. α_{gas} is kept at 2.21 ± 0.05. From the NFW formula, $R_{500}/R_{500} \approx 0.7$ and $R_{100}/R_{200} \approx 1.32$. As we noted earlier, the fact that the locations of R_{200} or R_{100} are imprecise is not a concern, because we are interested in the behavior of the baryon fraction in the vicinity of each radius. For example, whether the cluster reaches the cosmic baryon fraction at 0.95 or $1.05R_{100}$ makes little difference. This effect is small compared with the effect of varying α_{gas} on which f^{gas} is exponentially dependent.

The stellar fraction is assumed to stay constant at these large radii. Each mass bin has a distinct stellar fraction which, after extrapolating the gas fractions, is added to obtain the total baryon fraction. All calculations include an ICL contribution of

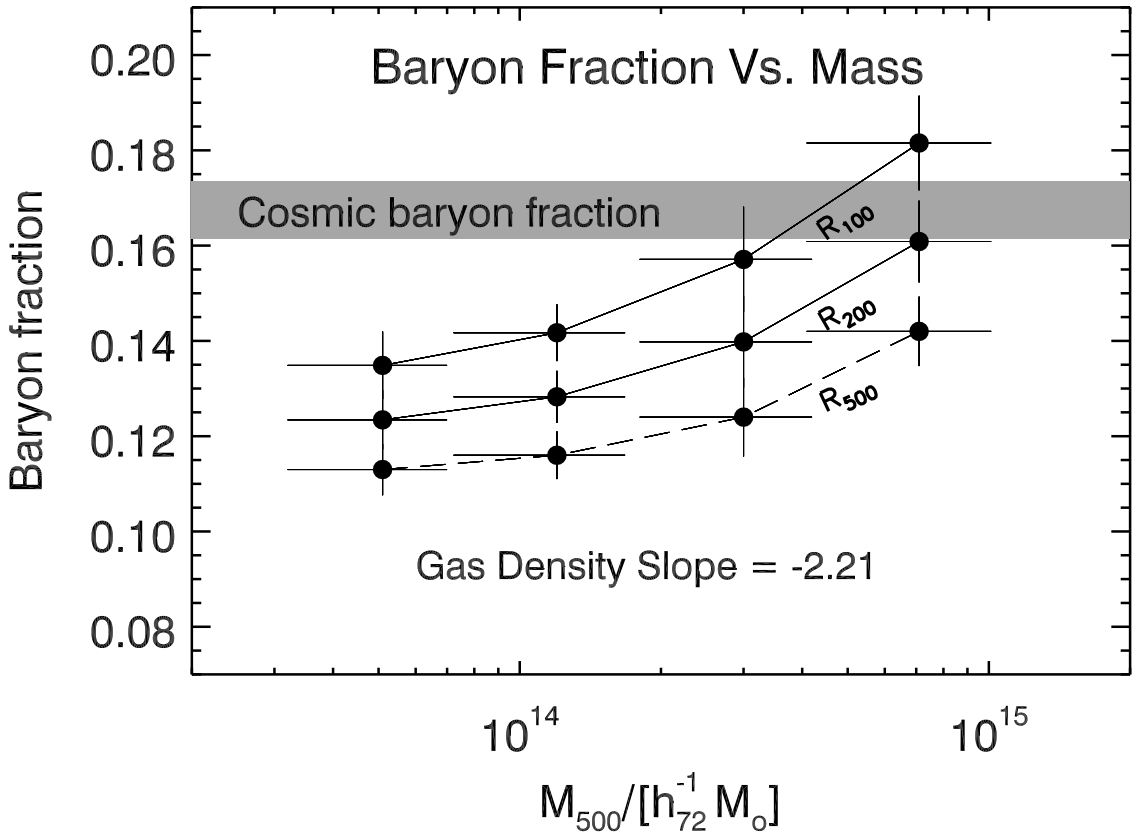

Figure 3.1: Cluster baryon fractions extended to R_{200} and R_{vir} under FIXED SLOPE SCENARIO, assuming fixed gas density slope $= -2.21 \pm 0.05$. This figure is drawn by extrapolating the gas fractions observed at R_{500}, and then adding a fixed stellar fraction at all radii. Note that the data point for the highest mass bin at R_{vir} is a "mock" point. The clusters are not expected to possess more than the cosmic baryon fraction. This data point just means that the highest mass clusters reach the cosmic baryon fraction at a radius smaller than R_{vir}.

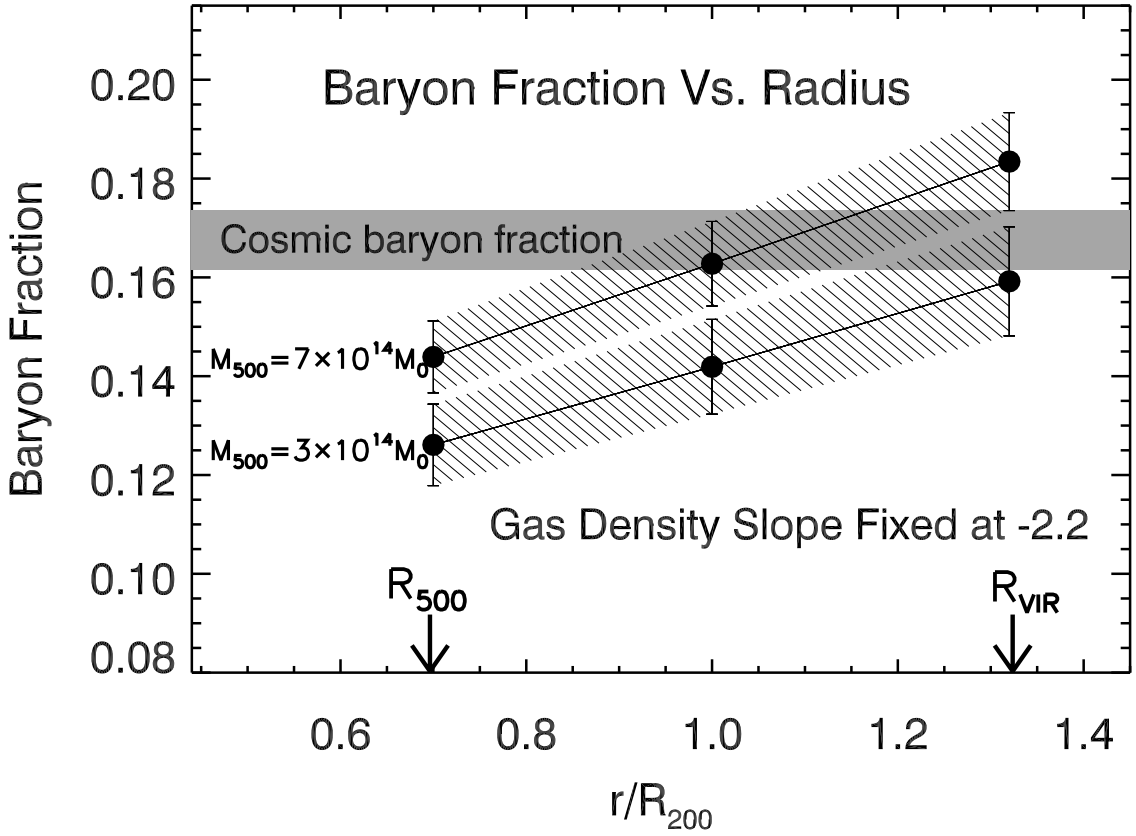

Figure 3.2: Baryon fractions for the two richest mass bins extended to R_{200} and R_{vir} under AVERAGE SCENARIO, assuming fixed gas density slope $= -2.21 \pm 0.05$. This figure is drawn by extrapolating the gas fractions observed at R_{500}, and then adding a fixed stellar fraction at all radii. The highest mass clusters reach the cosmic baryon fraction at a radius smaller than R_{vir}.

10% of the galactic stars.

This exercise of keeping the gas density slope fixed at from $R_{500} - R_{vir}$ also serves as a simple check to see whether it is possible to reach the cosmic baryon fraction of 0.1675 ± 0.006 from a scenario in which the slope does NOT stay fixed (or, in other words, steepens). A scenario with steepening of α_{gas} will obviously yield a lower estimate of the extrapolated baryon fraction than a scenario with fixed α_{gas}. If the fixed scenario fails to reach the cosmic baryon fraction at sufficiently large radii, then we do not expect the baryon fraction to reach the cosmic value under any steepening scenario. Figures 3.1 and 3.2 show that under this fixed slope scenario—suggested by some observations—the richest clusters reach the cosmic baryon fraction well before the virial radius, at $\sim R_{200}$. The results also show that poorer clusters, with $M_{500} \approx 3 \times 10^{14} M_{\odot}$, reach the cosmic baryon fraction at the virial radius. Clusters with lower masses do not reach the cosmic baryon fraction at the virial radius and might require further extrapolation.

Figure 3.3 represents the NFW TREND, i.e., gas density slope steepening to -2.4 ± 0.05 at R_{100}, following the trend of the NFW profile. Figure 3.4 represents the CONSERVATIVE SCENARIO, i.e., gas density slope steepening to -2.6 ± 0.05 at R_{100} to follow the observed trend suggested by Ettori and Balestra [2009]. Both the gas fraction and the baryon fraction are shown for R_{200} and R_{100}, respectively.

Under the NFW TREND (Figure 3.3), the mean baryon fraction of the richest clusters reaches the cosmic baryon fraction roughly midway between R_{200} and the virial radius (R_{100}). Poorer clusters ($M_{500} \approx 3 \times 10^{14} M_{\odot}$) also come within 1σ of the cosmic baryon fraction at R_{vir}. The least massive clusters do not reach the cosmic baryon fraction until beyond the virial radius. At the virial radius they contain $\sim$ 80% of the cosmic baryon fraction.

It can seen from Figure 3.4 that even under the CONSERVATIVE SCENARIO, where the gas density slope steepens to -2.6 ± 0.05 at R_{100}, the mean baryon fraction of the massive clusters ($\sim 7 \times 10^{14} M_{\odot}$) reaches the cosmic baryon fraction at roughly R_{vir}. Poorer clusters ($\sim 3 \times 10^{14} M_{\odot}$) reach roughly 85% of the cosmic baryon fraction at the virial radius, and lowest mass groups reach roughly 75% of the cosmic baryon fraction at the virial radius.

Figures 3.5 and 3.6 show the results of the NFW SCENARIO and CONSERVATIVE SCENARIO put together, for R_{200} and $R_{vir}(R_{100})$, respectively. Figure 3.5 shows the results for R_{200}, and Figure 3.6 for R_{100}. The solid line in each plot represents the CONSERVATIVE SCENARIO in which the gas density slope α_{gas} steepens incrementally from 2.21 ± 0.05 at R_{500} to 2.6 ± 0.05 at R_{100}. The dashed line is the NFW TREND which follows a similar steepening to the NFW profile, i.e., α_{gas} steepens incrementally from 2.21 ± 0.05 at R_{500} to 2.4 ± 0.05 at R_{100}. In both scenarios α_m for the NFW profile steepens incrementally from 2.57 at R_{500} to 2.74 at R_{100}. Fixed stellar fractions for each mass bin (Table 2.5), including the ICL (10% of galactic stellar mass), have been added to f^{gas} at all radii.

Figure 3.7 shows the baryon fraction as a function of radius for the CONSERVATIVE SCENARIO and NFW TREND. Only the two largest mass bins, i.e., $M_{500} = 7.1 \times 10^{14} M_{\odot}$ and $M_{500} = 3.0 \times 10^{14} M_{\odot}$ are shown.

Figure 3.7 is achieved by extrapolating the gas fraction at each interval, using the same scaling as in Equation 3. The baryon fraction at a radius R_i is found from extrapolating the gas fraction at a baseline radius R_0 using:

$$f^{gas}(R_i) = f^{gas}(R_0) \left(\frac{R_i}{R_0} \right)^{\alpha_m - \alpha_{gas}} \tag{3.4}$$

and then adding the stellar fraction for that mass to the gas fraction. The error

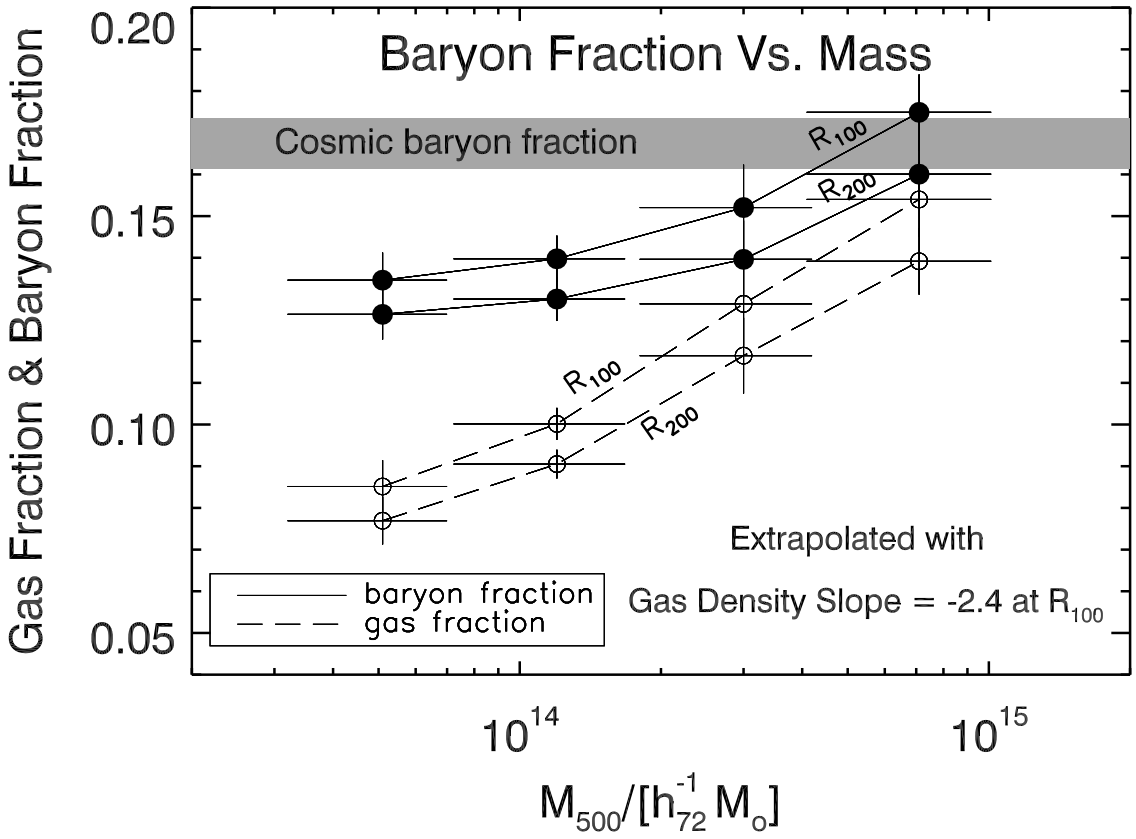

Figure 3.3: Baryon fraction at R_{200} and R_{vir} under the NFW TREND, where the gas density slope steepens to -2.4 ± 0.05 at R_{100}. The mean baryon fraction of the bin with the richest clusters reaches the cosmic baryon fraction roughly midway between R_{200} and R_{100}. Clusters in the next to largest mass bin ($3 \times 10^{14} M_{\odot}$) also come within 1σ of the cosmic baryon fraction at R_{vir}. Clusters lower than that do not reach the cosmic baryon fraction until beyond the virial radius.

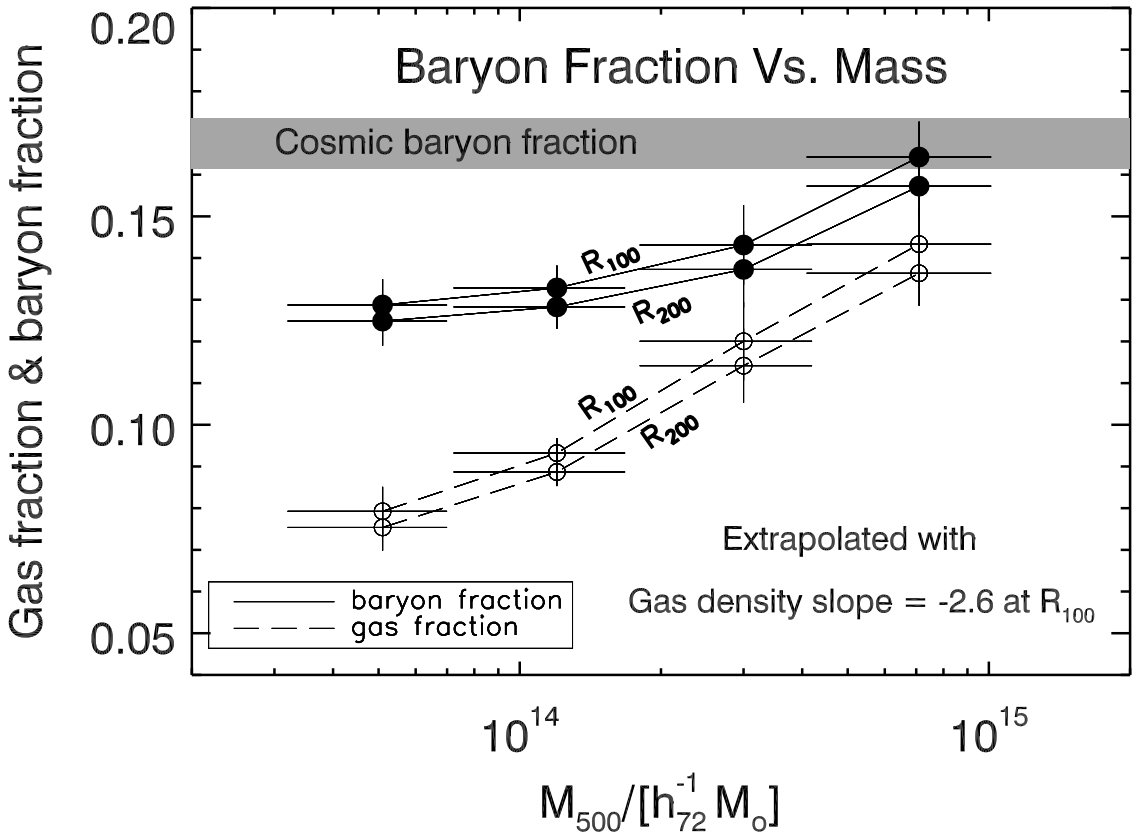

Figure 3.4: Baryon fraction at R_{200} and R_{vir} under the CONSERVATIVE SCENARIO, where the gas density slope steepens to -2.6 ± 0.05 at R_{100}. Even in this scenario, the mean baryon fraction of the bin with the richest clusters ($\sim 7 \times 10^{14} M_{\odot}$) reaches the cosmic baryon fraction at roughly R_{vir}. Lower mass clusters are still 1σ or more below the cosmic baryon fraction at R_{vir}.

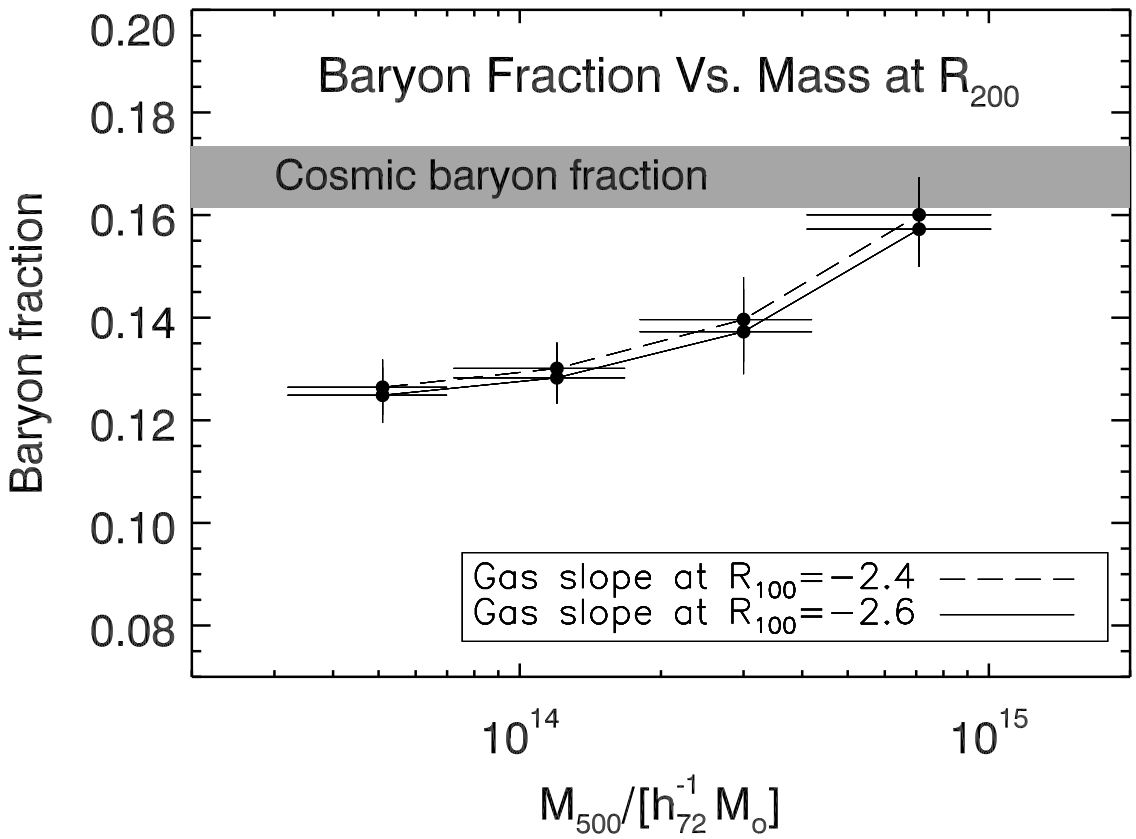

Figure 3.5: Baryon fraction extrapolated to R_{200} under each of the CONSERVATIVE SCENARIO (solid) and NFW TREND (dashed).

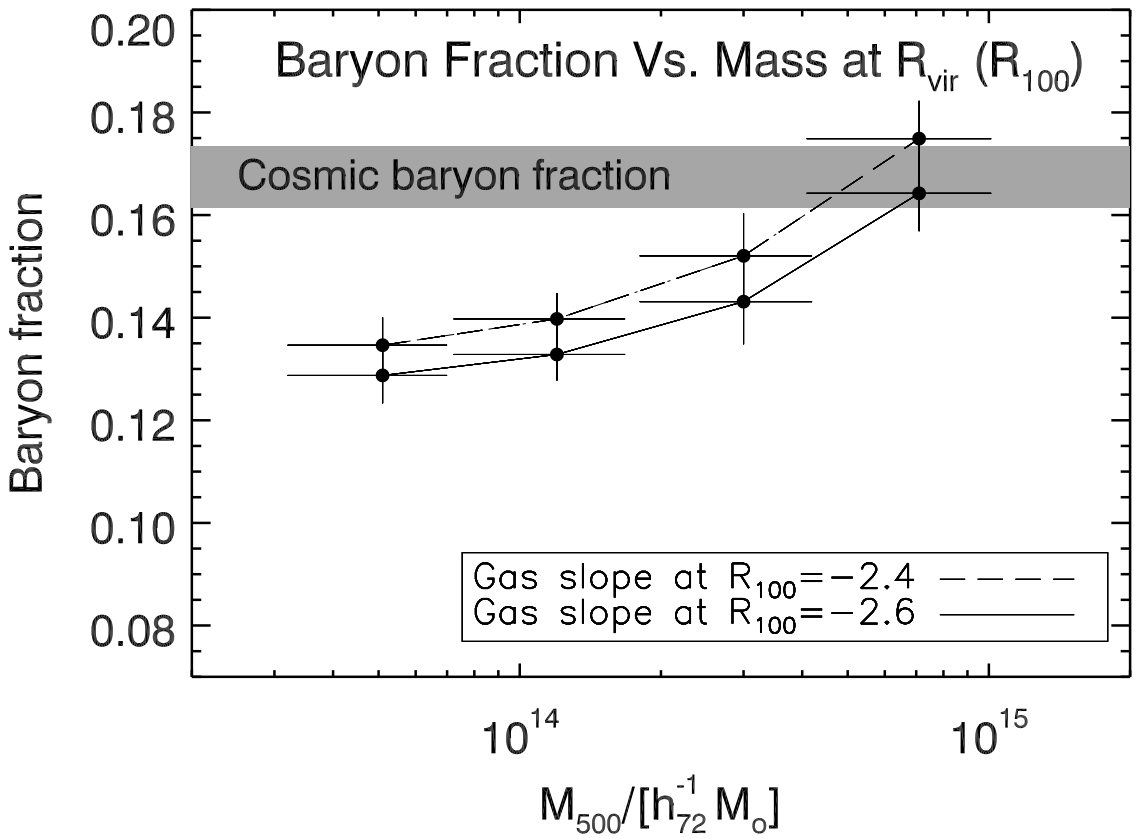

Figure 3.6: Baryon fraction extrapolated to $R_{vir} = R_{100}$ under each of the CONSERVATIVE SCENARIO (solid) and NFW TREND (dashed).

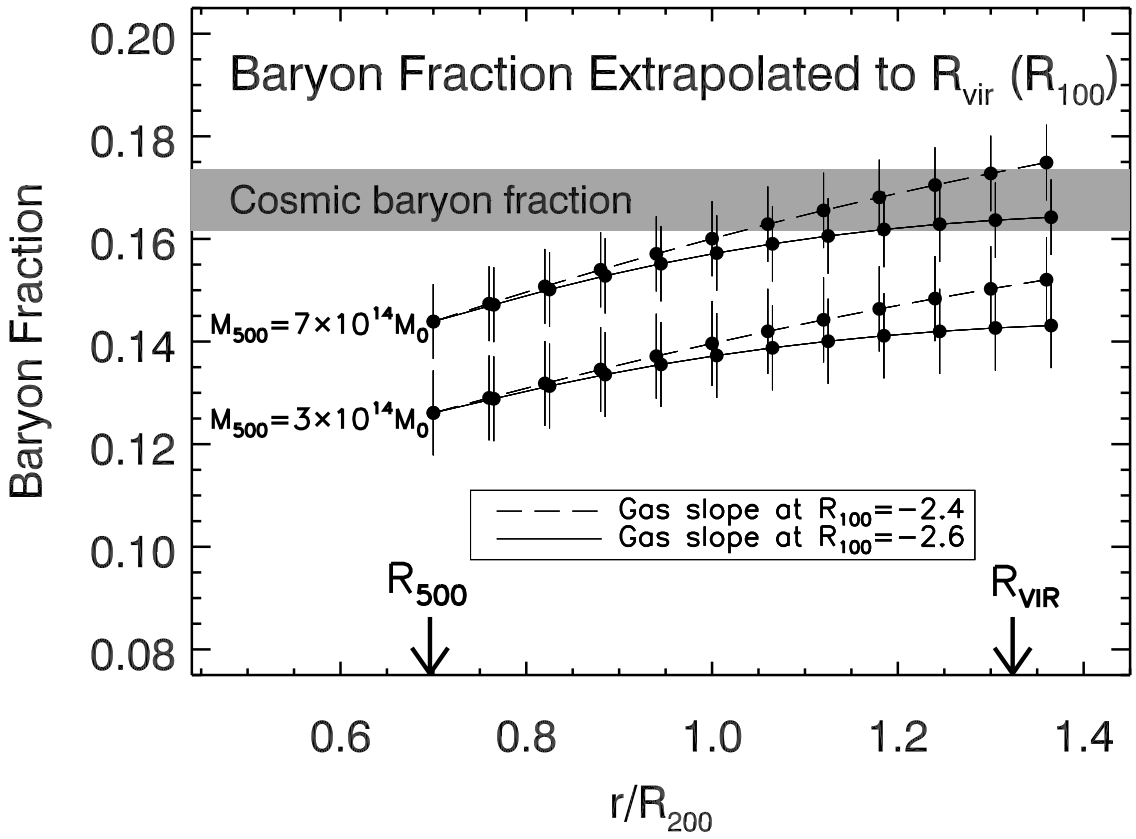

Figure 3.7: Baryon fraction extrapolated under the CONSERVATIVE SCENARIO and NFW TREND. Only the two largest mass bins, i.e., $M_{500} = 7.1 \times 10^{14} M_{\odot}$ and $M_{500} = 3.0 \times 10^{14} M_{\odot}$ are shown.

in $f^{baryons}$ is found from adding the errors in gas fraction and stellar fraction in quadrature (see Equation 2.20).

3.0.1 Error Analysis

There are two sources of error in the extrapolated gas fraction at a radius R_i: the gas density slope α_{gas} and the gas fraction at the baseline radius, R_0. Therefore, the error in gas fraction at R_1 is found from a propagation of errors in α_{gas} and the gas fraction at R_0, respectively. Since the two factors multiply in Equation 3.4, their fractional errors add in quadrature:

$$\frac{\Delta f^{gas}(R_i)}{f^{gas}(R_i)} = \sqrt{\left(\frac{\Delta f^{gas}(R_0)}{f^{gas}(R_0)}\right)^2 + \left(\frac{\Delta (R_i/R_0)^{\alpha_m - \alpha_{gas}})}{(R_i/R_0)^{\alpha_m - \alpha_{gas}}}\right)^2} \tag{3.5}$$

We assume that there is no error in the NFW slope—since there is an analytical formula for it—nor in the values of R_{500}, R_{200} and R_{vir}.

The uncertainty in $(R_i/R_0)^{\alpha_m - \alpha_{gas}}$ can be calculated using the following formula for exponential error propagation (found in any statistics textbook). If

$$Z = A^n, \tag{3.6}$$

then

$$\Delta Z = \left(\frac{\delta Z}{\delta n}\right) \Delta n = A^n \ln A \Delta n. \tag{3.7}$$

Therefore,

$$\Delta (R_i/R_0)^{\alpha_m - \alpha_{gas}} = (R_i/R_0)^{\alpha_m - \alpha_{gas}} \ln(R_i/R_0) \Delta(\alpha_m - \alpha_{gas}) \tag{3.8}$$

where $\Delta(\alpha_m - \alpha_{gas}) = \Delta\alpha_{gas} = 0.05$.

3.0.2 Summary of Results

Our analysis shows that the baryon fraction in clusters increases beyond R_{500} for all cluster masses. The most massive clusters ($M_{500} \sim 7 \times 10^{14} M_{\odot}$) reach the cosmic baryon fraction typically at $R_{vir} \pm 20\%$. The less massive clusters and groups reach roughly 75–85% of the cosmic baryon fraction at the virial radius. It would probably require further extrapolation to see all the baryons in poor clusters.

Table 3.1: Extrapolated Gas Fraction of Massive Clusters

	$\alpha_{gas,100} = 2.2$	$\alpha_{gas,100} = 2.4$	$\alpha_{gas,100} = 2.6$
R_{500}	0.123 ± 0.007	0.123 ± 0.007	0.123 ± 0.007
R_{200}	0.142 ± 0.008	0.139 ± 0.008	0.136 ± 0.008
R_{vir}	0.162 ± 0.009	0.154 ± 0.009	0.143 ± 0.008

The values of the baryon fraction of the most massive clusters ($M_{500} \approx 7 \times 10^{14} M_{\odot}$), at R_{500}, R_{200} and R_{100}, under three scenarios of extrapolation: from left, the Fixed Slope Scenario where α_{gas} remains fixed at 2.2 up to the virial radius; the NFW Trend where α_{gas} steepens to 2.4 at R_{vir}; and the Conservative Scenario where α_{gas} steepens to 2.6 at R_{vir}.

Table 3.2: Extrapolated Baryon Fraction of Massive Clusters

	$\alpha_{gas,100} = 2.2$	$\alpha_{gas,100} = 2.4$	$\alpha_{gas,100} = 2.6$
R_{500}	0.143 ± 0.007	0.143 ± 0.007	0.143 ± 0.007
R_{200}	0.163 ± 0.009	0.160 ± 0.007	0.157 ± 0.007
R_{vir}	0.183 ± 0.010	0.175 ± 0.007	0.164 ± 0.007

The values of the gas fraction of the most massive clusters ($M_{500} \approx 7 \times 10^{14} M_{\odot}$), at R_{500}, R_{200} and R_{100} under three scenarios of extrapolation: from left, the Fixed Slope Scenario where α_{gas} remains fixed at 2.2 up to the virial radius; the NFW Trend where α_{gas} steepens to 2.4 at R_{vir}; and the Conservative Scenario where α_{gas} steepens to 2.6 at R_{vir}. This just represents Figure 3.0.2 with a constant stellar fraction of 0.021 ± 0.002 added at each radius (Giodini et al. [2009]). This includes ICL, assumed to be 10% of the stellar fraction.

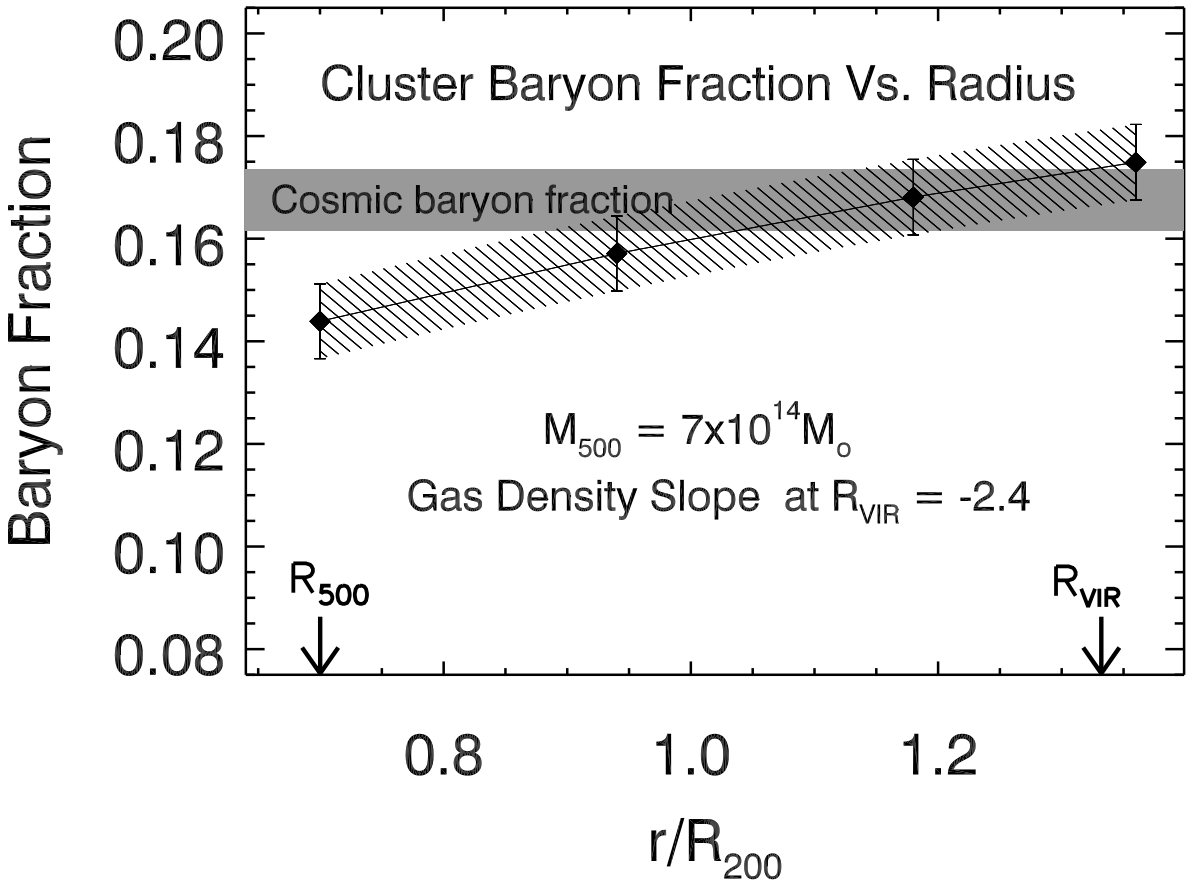

Figure 3.8: Baryon fraction extrapolated under the NFW TREND scenario, where the gas density slope follows the relative steepening of the NFW slope, and which we consider to be the most realistic scenario. α_{gas} steepens from 2.21 ± 0.05 at $R_{500}$to 2.4 ± 0.05 at R_{vir}. Only the largest mass range $M_{500} = 7.1 \times 10^{14} M_{\odot}$ is shown.

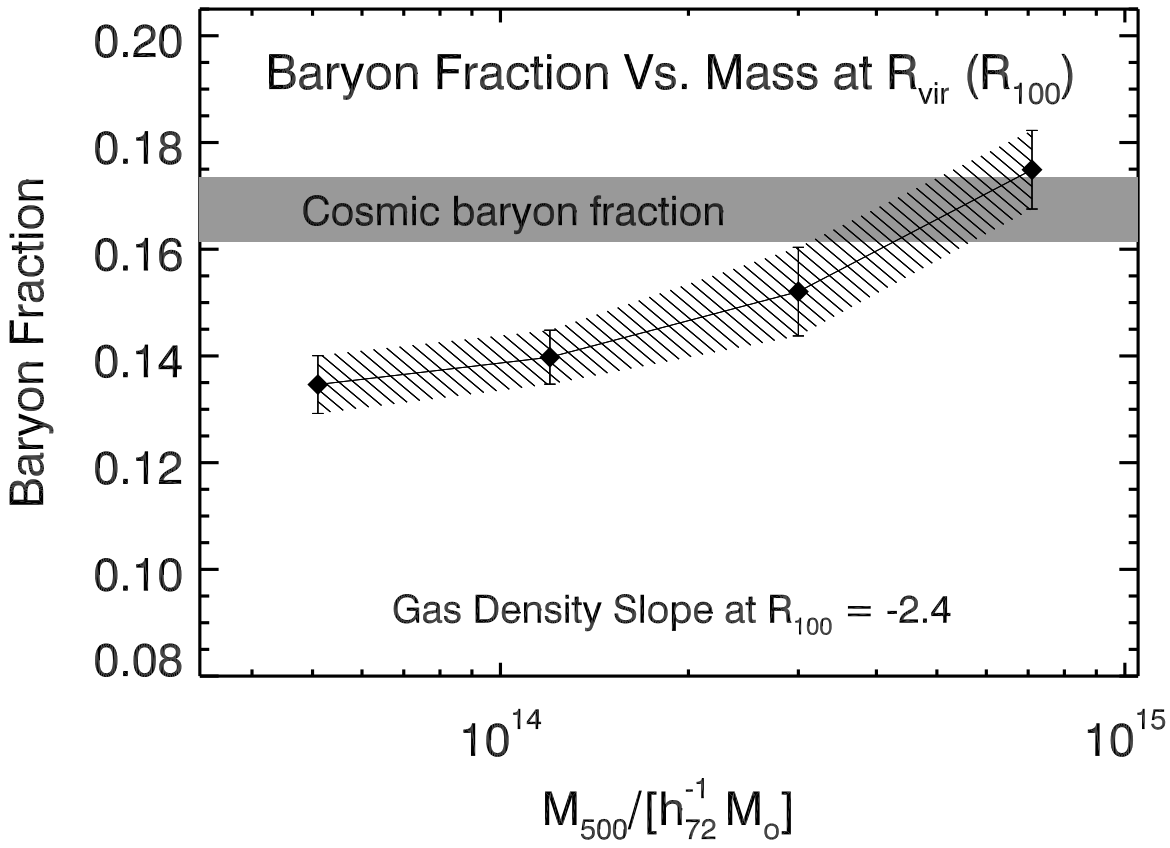

Figure 3.9: Baryon fraction extrapolated to $R_{vir} = R_{100}$ under the NFW TREND scenario, where the gas density slope follows the relative steepening of the NFW slope. α_{gas} steepens from 2.21 ± 0.05 at R_{500} to 2.4 ± 0.05 at R_{vir}.

Chapter 4

Discussion of Results

In this chapter we will discuss some of the assumptions and caveats that underlie our analysis. Then, with a fuller understanding of our results, we will discuss to what extent the current theories of the dynamics of intracluster gas explain our results.

First, we assumed that both the NFW profile and the gas density profile smoothly continue their observed profile to R_{vir}. In particular, we used several observations at R_{200} (Plagge et al. [2009], Ettori and Balestra [2009], Dai et al. [2009]), and we assumed that the trends observed at R_{200} would continue from R_{200} to R_{vir}. If cluster gas density profiles show discontinuous behavior for whatever reason beyond R_{200}, our analysis will need modification. For example, if there is an abrupt, steep decline in the gas density at any radius beyond R_{500}, the cluster may reach the cosmic baryon fraction either farther beyond R_{vir} or not at all. (For example, see Dai et al. [2009] (Figure 2.4) who report a sudden, sharp fall in X-ray surface brightness at about R_{200} for their richest stacked clusters.) On the other hand, if the gas density slope becomes flatter beyond R_{200}, then the cluster might reach the cosmic baryon fraction at a smaller radius than we predict. (For example, see the very shallow, $\sim r^{-2}$ gas density profile reported by George et al. [2009] to R_{vir}.)

Another implicit assumption in our analysis is that the gas density profile is

roughly the same for the full cluster mass range of our sample. We derived the value of the β parameter from observations of massive clusters and applied them to the full sample. Observations of the gas density slope in groups are few (Dai et al. [2009], Vikhlinin et al. [2006]) and in general appear to indicate shallower slopes in groups ($\alpha_{gas} \sim 1.8$ at $\sim R_{200}$) than in massive clusters. If so, then f^{gas} in groups would rise faster per unit radius than in rich clusters, and the baryon fraction as a function of mass at virial radius would be flatter than in our analysis. Much work needs to be done and better resolution in imaging is needed so that the contents of groups at large radii can be understood better.

Another parameter which could potentially vary is the concentration parameter. We took the mean value of c_{200} from weak lensing measurements by Mandelbaum et al. [2008], which was about 5 for our mass range (see Figure 2.1). As Mandelbaum et al. [2008] discuss in their paper, this value is slightly lower than results from simulations and some previous studies. If c_{200} was higher than 5, the clusters would be more concentrated. The NFW profile would then fall off more sharply relative to the gas density profile, causing the gas fraction to rise even further per unit of radius than for $c_{200} = 5$. The effect is small, however, and a change of c_{200} to 7 induces a change in baryon fraction of merely 5%. In addition, the NFW TREND scenario of our analysis assumes that the gas density profile follows the same trend of steepening as the NFW beyond R_{500}, in which case the effects will nearly cancel out.

Another possible source of error is inconsistency in the methods of total mass calculation across observations. To find stellar fraction, Giodini et al. [2009] use weak lensing to calculate total mass of their sample of COSMOS clusters. Lin et al. [2003] use an $M - T_X$ relation based on weak lensing (Pratt et al. [2009]) to estimate total mass. However, to find the gas fraction, Vikhlinin et al. [2006], Arnaud et al. [2007] and Sun et al. [2009], use the assumption of hydrostatic equilibrium to calculate total mass. Hydrostatic equilibrium assumes that gravity in clusters is balanced by thermal

pressure. This allows us to estimate total gravitational mass from X-ray data, since X-ray data yields a measure of total thermal pressure in a cluster (temperature times gas density). However, this method may lead to an underestimate of mass, since non-thermal pressure may also contribute to balancing gravity. Nagai et al. [2007] estimate from simulations that for high mass clusters, the assumption of hydrostatic equilibrium led to a 10% underestimate of total mass. In the case of groups, the discrepancy could be as large as 45%. If mass has been underestimated, it follows that gas fraction has been overestimated. Consistent methods of total mass detection need to be used for observations of gas and stellar fraction.

We have four sets of observations for the stellar fraction in clusters, and they are significantly discepant. We expressed in Section 2.3 our concerns about putting together data from COSMOS (Giodini et al. [2009]) and 2MASS (Lin et al. [2003]) on the same plot. Each sample covers a mass range of only one order of magnitude: COSMOS clusters range from $10^{13} - 10^{14} M_{\odot}$, and 2MASS clusters range from $10^{14} - 10^{15} M_{\odot}$. Individually, each mass range is too small to exhibit a reliable correlation of f^{stars} with M_{500}. We must put the two together. But the two sources use different methods to calculate the total mass of their clusters: Giodini et al. [2009] use weak lensing whereas Lin et al. [2003] use the $M - T_X$ scaling relations found from weak lensing (Pratt et al. [2009]). It is possible that there is a systematic discrepancy between the two methods. Each sample, taken by itself, shows a weak trend with mass with a large scatter. Combined by Giodini et al. [2009], the trend becomes steeper with a smaller error bar, but this could be caused by a slight shift of one of the two samples. One the other hand, there is considerable overlap in the two samples which is reassuring.

The other observations for stellar fraction differ slightly from the results above. Gonzalez et al. [2007] observe a slightly steeper trend of f^{stars} with M_{500} than Giodini et al. [2009] and Lin et al. [2003]. This might be because their sample is biased towards

groups and clusters with large brightest cluster galaxies (BCG). Andreon [2010] find total mass from caustic analysis which may be less accurate than lensing. However, while the stellar fraction versus mass relations differ somewhat among observations, their contribution to total baryon fraction is small and will not cause major changes on our main conclusions. For example, a steeper stellar fraction would add stars to low mass clusters and reduce their discrepancy from the cosmic baryon fraction at the virial radius, but not by a significant amount. Similarly, if we use a larger contribution of the ICL—say, 20%, the upper bound reported by Zibetti [2008]—then the baryon fraction would rise everywhere by roughly 1%.

Why is the baryon fraction lower than the cosmic value for all masses at R_{500}, and in low masses even at R_{100}? As we mentioned in the introduction, this suggests heating of the intracluster gas which causes the gas to expand to radii larger than R_{500}. A few mechanisms are gravitational shock-heating, energy transfer from dark matter, star formation, AGN and supernovae, and possibly other, less understood phenomena such as thermal evaporation and pre-heating.

The fundamental fact is that accretion of gas from large scales inward results in shock-heating which causes gas to heat up and expand to outer radii. The dark matter, being collisionless, does not get shock-heated (Takizawa and Mineshige [1998] and references therein). This effect results in an ICM profile more spread-out than the dark matter profile, as has been seen in observations. It implies that even if there were no star formation nor any energy input, we might still fail to see all the gas at R_{500}.

Another factor which contributes to gas depletion in virialized structures is the transfer of energy from dark matter to gas during mergers. Dark matter can lose up to 10% of its energy in an equal mass collision; McCarthy et al. [2007] show that even a 10:1 mergers causes the dark matter to lose a couple of percent of its energy

to gas. This should cause the gas to expand to outer radii. Simulations show that such mergers are common: Cohn and White [2005] calculate that a typical cluster will undergo four 5:1 accretion events since $z \sim 2$, and Fakhouri and Ma [2008] show that the mean rate for 10:1 or larger mergers in clusters has been roughly two per halo per unit redshift. Simulations have estimated the magnitude of this effect. For simulations with no star formation or radiative processes, Crain et al. [2007] find that the average baryon fraction within R_{200} is 90% of the cosmic mean at $z = 0$, probably due to this effect.

However, all these processes are scale-free, i.e., should affect low and high mass systems to the same degree. Any explanation of our results must address the question of why the baryon fraction is lower in groups than in clusters. One part of the answer is, of course, that small groups are unable to retain hot gas because of their smaller gravitational potential wells. However, if the heating was simply because of gravitational infall (shock-heating), then lower mass systems, being small, should have less of it than higher mass systems. Thus the fraction of gas which gravitationally heats up and expands should be the same for all masses. There seem to be sources of additional energy which cause the gas to be kicked out preferentially from low-mass clusters, and cause the baryon fraction to be scale-dependent.

Another way of putting the question is the following. It seems as if the variation of gas fraction—from low in groups to high in clusters—does not fully complement the variation of stellar fraction—from high in groups to low in clusters. One would guess that if star formation is more efficient in lower mass systems than in rich clusters(Lin et al. [2003], Giodini et al. [2009], Gonzalez et al. [2007], Andreon [2010]), there is less gas left in the lower mass systems than in rich clusters, and thus the total should be roughly constant across the full mass range. However, the total baryon fraction as a function of halo mass, even at R_{500}, is not flat, allowing for the possibility of additional energy inputs.

Star formation removes the most bound gas with the lowest cooling times, leaving behind gas with a higher mean entropy than before (Voit and Bryan [2001], Tozzi and Norman [2001], Voit et al. [2002]). This gas is less gravitationally bound and more susceptible to escape. This can be seen in simulations: if, for example, 10% of gas is made to form stars, the resulting decrease in gas fraction is more than 10% (Bode et al. [2009]). By this effect, if star formation is more common in low mass systems, this would cause a bigger fraction of the remaining gas to escape from the groups than from the clusters. This is one possible explanation of the scale-dependence of the baryon fraction.

Another source of non-gravitational energy in clusters is heating by galactic AGN and supernovae (Cavaliere and Fusco-Femiano [1978], Metzler and Evrard [1994], Valdarnini [2003], Sijacki et al. [2008], and references therein). This energy input can be made scale-dependent under the reasonable assumption that the greater the stellar mass in galaxies, the larger the number of supernovae and AGN. Then, since stellar fraction in groups is higher than in clusters, the energy input from supernovae and AGN will be fractionally larger in groups than in clusters, causing a greater fraction of gas to heat up and expand outward in groups than in clusters.

Note that there is a degeneracy in these two effects. Not only do they both work in the same direction, but both depend on the exact scaling of the stellar fraction with mass. Simulations have been done to test whether these effects together can explain the trend in baryon fraction. When Nagai et al. [2007] try to match their simulated clusters to the Chandra observations of gas fraction (Vikhlinin et al. [2006], Sun et al. [2009]), they find that in order to match the observed scaling of gas fraction with radius, they must make many more stars than have been observed in clusters. This is known as the "overcooling problem".

However, the observations we have used in our analysis are not the same as those used by Nagai et al. [2007]. We used XMM-Newton observations as well as Chandra

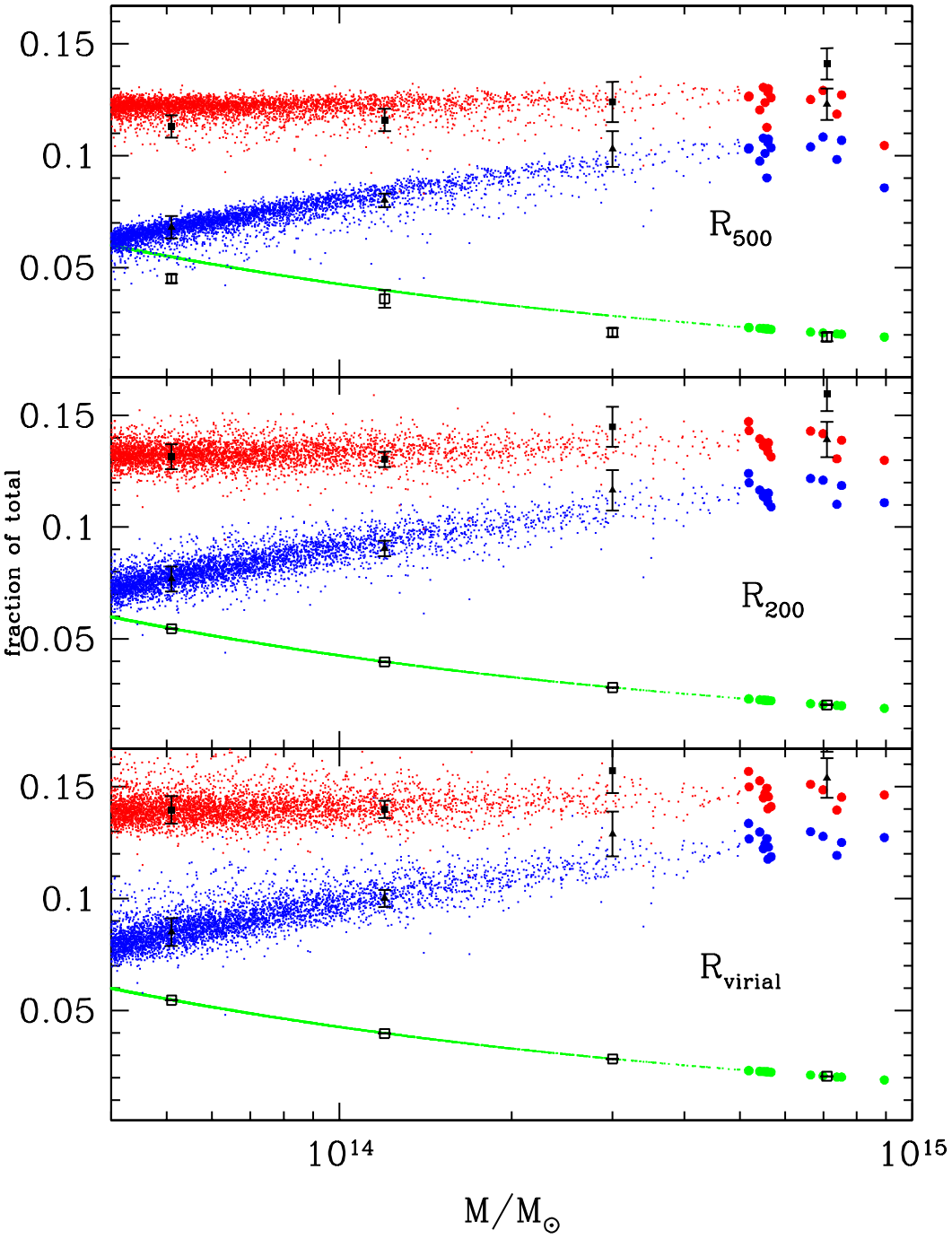

Figure 4.1: The comparison of our results using the NFW Trend scenario at R_{500}, R_{200} and R_{vir} (black data points) with the predictions of Bode et al. [2009]'s simulations. Green points represent stellar fraction, blue points represent gas fraction, and red points represent total baryon fraction. Bold points are massive simulated clusters for better visibility. There is good agreement between observations and simulations for low mass clusters. But massive clusters are observed to possess more gas than expected from simulations even at R_{500}.

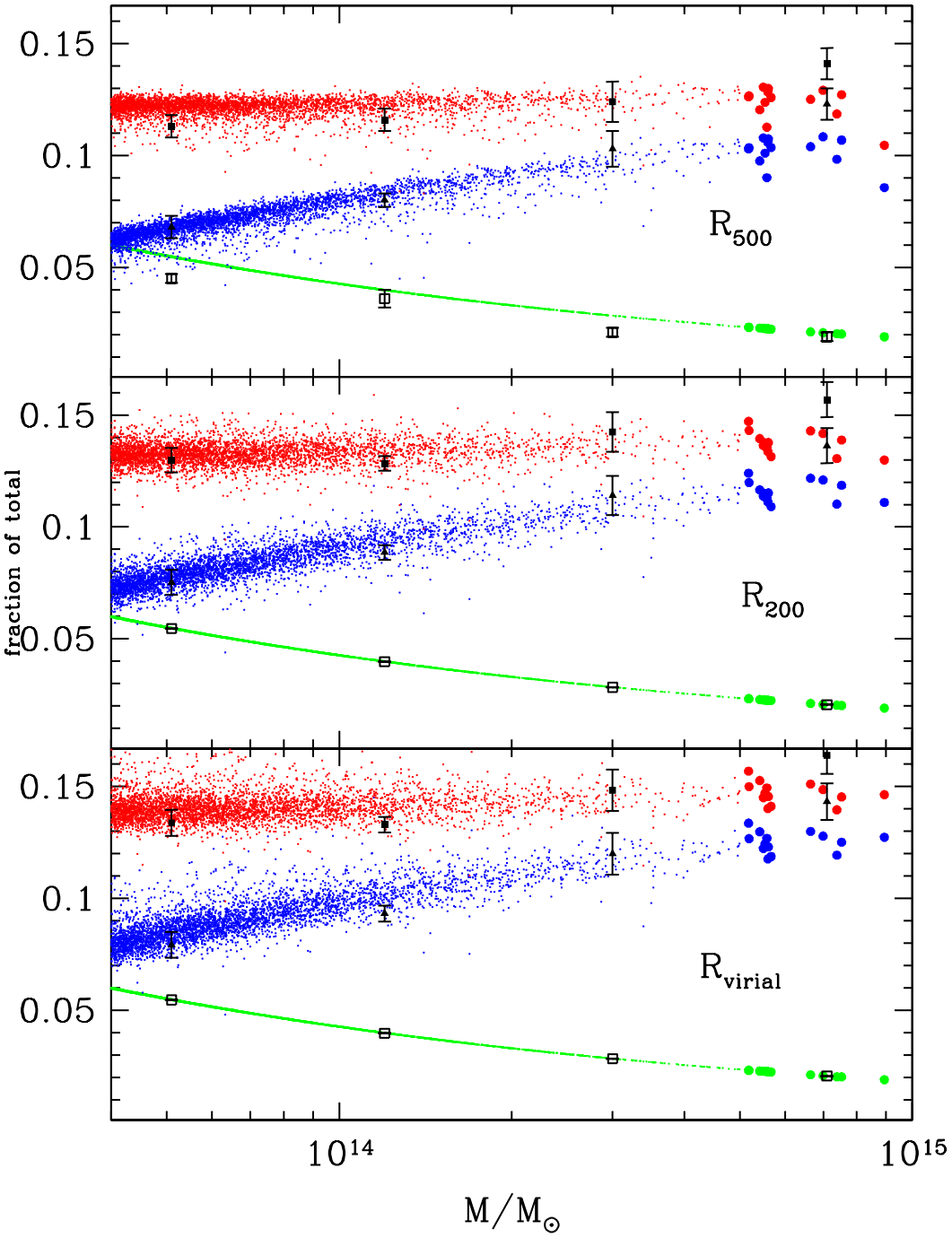

Figure 4.2: The comparison of our results using the Conservative Scenario at R_{500}, R_{200} and R_{vir} (black data points) with the predictions of Bode et al. [2009]'s simulations. Green points represent stellar fraction, blue points represent gas fraction, and red points represent total baryon fraction. Bold points are massive simulated clusters for better visibility. There is good agreement between observations and simulations for low mass clusters. But massive clusters are observed to possess more gas than expected from simulations even at R_{500}. In general this scenario fits better than the NFW Trend.

to constrain gas fraction, and we used COSMOS and 2MASS data of Lin et al. [2003] and Giodini et al. [2009] to constrain the stellar fraction. To test whether the above mechanisms can explain our observations, we compared our results with Bode et al. [2009]'s model for cluster formation. In this model, clusters start with the cosmic baryon fraction, undergo gravitational shock-heating, energy transfer from dark matter to baryons, and galaxy formation. The model takes the stellar fraction versus mass scaling relation as an input parameter. We input the stellar fraction scaling relation obtained from the combined samples of Lin et al. [2003] and Giodini et al. [2009]:

$$f_{500}^{stars} = 5.5^{+0.1}_{-0.1} \times 10^{-2} \left(\frac{M_{500}}{5 \times 10^{13} M_{\odot}} \right)^{-0.37 \pm 0.04} \tag{4.1}$$

The model includes the effects of energy feedback from star formation, AGN and supernovae, non-thermal pressure (such as bulk motion), and a 5% transfer of binding energy from dark matter to baryonic matter during structure formation. Of these effects, star formation and feedback can be scale-dependent.

The result of the comparison was Figures 4.1 and 4.2, corresponding to two of our two extrapolations scenarios. With the given stellar fraction, the predictions of the model for gas fraction and baryon fraction fit well with low mass clusters and groups. However, for the highest mass clusters, observations show a significantly higher gas and baryon fraction than simulations predict even at R_{500} (top panel). The lower two panels show the comparison of our extrapolated baryon fraction with the predictions from Bode et al. [2009]'s simulations at R_{200} and R_{vir}, respectively. The discrepancy grows at larger radii. We did not even need to include feedback from AGN and SNe for this exercise; the star formation was high enough to lower the gas fraction to observed values in all cases but the richest clusters. Additional energy input, especially if it scales with mass, would deplete the gas in low mass clusters more than in the rich clusters. It would not raise the baryon fraction in rich clusters, which is the source

of disagreement. It seems that the high mass clusters retain more gas than expected in these models. Either energy sources are fewer than expected in large clusters, or they have a way of resisting extra energy input, or the observations overestimate the gas fraction for the richest clusters.

Chapter 5

Comparison with Previous Findings

One motivation for this paper is the claim made by previous observations that the baryon (or gas) gas fraction in clusters was well below the cosmic baryon fraction. We compare these observations with our results for the richest clusters; our results suggest that massive clusters reach the cosmic baryon fraction in the range of $R_{200} - R_{vir}$. This will indicate whether our extrapolation using the observed slopes agrees with observations of gas fraction at R_{200}, and whether or not we have a "missing baryon" problem.

For comparison with the cosmic baryon fraction, we present all observations in terms of baryon rather than gas fraction, i.e., we add the stellar contribution as observed in Section 2.3. In Figure 5.1 we show the gas fractions observed with Suzaku and AMiBA (George et al. [2009], Umetsu et al. [2009]), for $M_{500} \sim 7 \times 10^{14} M_{\odot}$ clusters, and add the stellar fraction observed for this range as derived from COSMOS and 2MASS data (0.021 ± 0.002 from Giodini et al. [2009], Lin et al. [2003]). The scenario used is NFW Trend, which we consider to be our most realistic scenario (i.e., the gas density profile slope steepens slightly beyond R_{500} in a similar relative

trend to the NFW profile).

Figure 5.1 shows that the gas fractions from Suzaku and AMiBA, when corrected for the stellar (and ICL) fraction (filled points), fit nicely with our extrapolated baryon fraction (shaded band), well within 1σ. This suggests that these clusters should reach the cosmic baryon fraction when observed to nearly the virial radius. The Chandra and XMM-Newton observations at R_{500} (Vikhlinin et al. [2006], Arnaud et al. [2007]) are also shown, which form baseline gas fraction at R_{500}.

We also compare our extrapolated baryon fraction with the WMAP 5-year results as analyzed by Afshordi et al. [2007], who claimed strong deficiency of baryons in clusters. The mass range of the cluster sample used by Afshordi et al. [2007] is lower than the mass range of Figure 5.1. So in Figure 5.2 we show the baryon fraction for a lower mass range, $M_{500} \sim 3 \times 10^{14} M_{\odot}$, which is more comparable with Afshordi et al. [2007]'s sample. The figure shows good agreement between our extrapolated baryon fraction (shaded band) and the baryon fraction derived from WMAP (red diamonds). The relevant stellar fraction has been added for this mass range (0.023 ± 0.002 from Giodini et al. [2009], Lin et al. [2003]). The baryon fraction for this mass range reaches the cosmic baryon fraction at slightly beyond R_{vir}. At R_{200}, the discrepancy in ($\sim 15\%$) is much smaller than that reported by Afshordi et al. [2007] (35–40%).

SZ-decrements from WMAP 7-year results have been recently analyzed by Komatsu et al. [2010]. They fit the SZ measurements of clusters to 'KS' profiles (Komatsu and Seljak [2001]) which are similar to the universal mass density profile of NFW, and thus assume hydrostatic equilibrium. Fitting to KS profiles, Komatsu et al. [2010] find that the SZ signal from the stacked cluster sample is 0.5–0.7 times the results of X-ray observations, and $f_{500}^{gas} \approx 0.125$, showing no clear dependence on total mass.

One reason for the systematically lower gas fraction resulting from KS profile-fitting than from X-ray observations could be the assumption of hydrostatic equi-

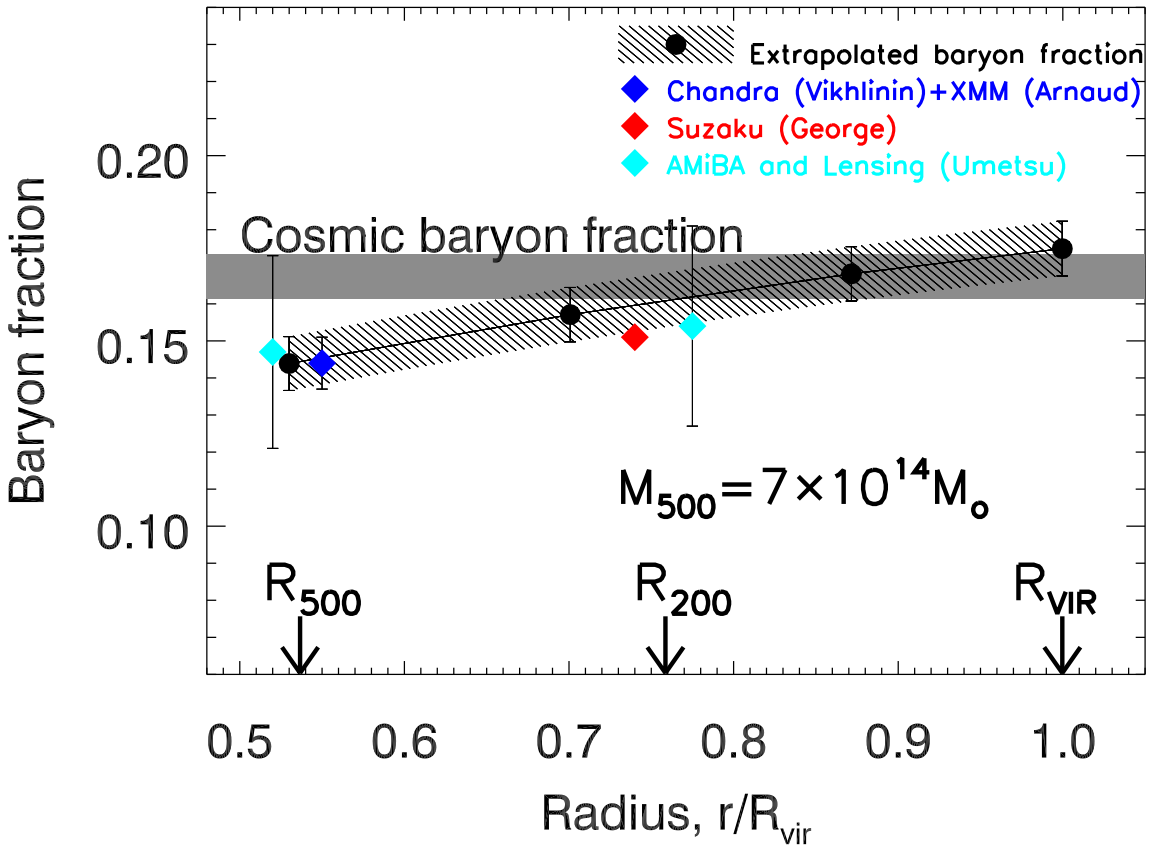

Figure 5.1: Comparison of extrapolated baryon fraction for $M_{500} \sim 7 \times 10^{14} M_{\odot}$, with observations from Suzaku and AMiBA (George et al. [2009] and Umetsu et al. [2009], respectively). The gas fractions from Suzaku and AMiBA, when corrected for the stellar fraction (filled points) (Giodini et al. [2009], Lin et al. [2003]) fit nicely with our extrapolated baryon fraction (shaded band), well within 1σ. The Chandra and XMM-Newton observations at R_{500} (Vikhlinin et al. [2006], Arnaud et al. [2007]) are also shown, which are the basis for our baseline gas fraction at R_{500}.

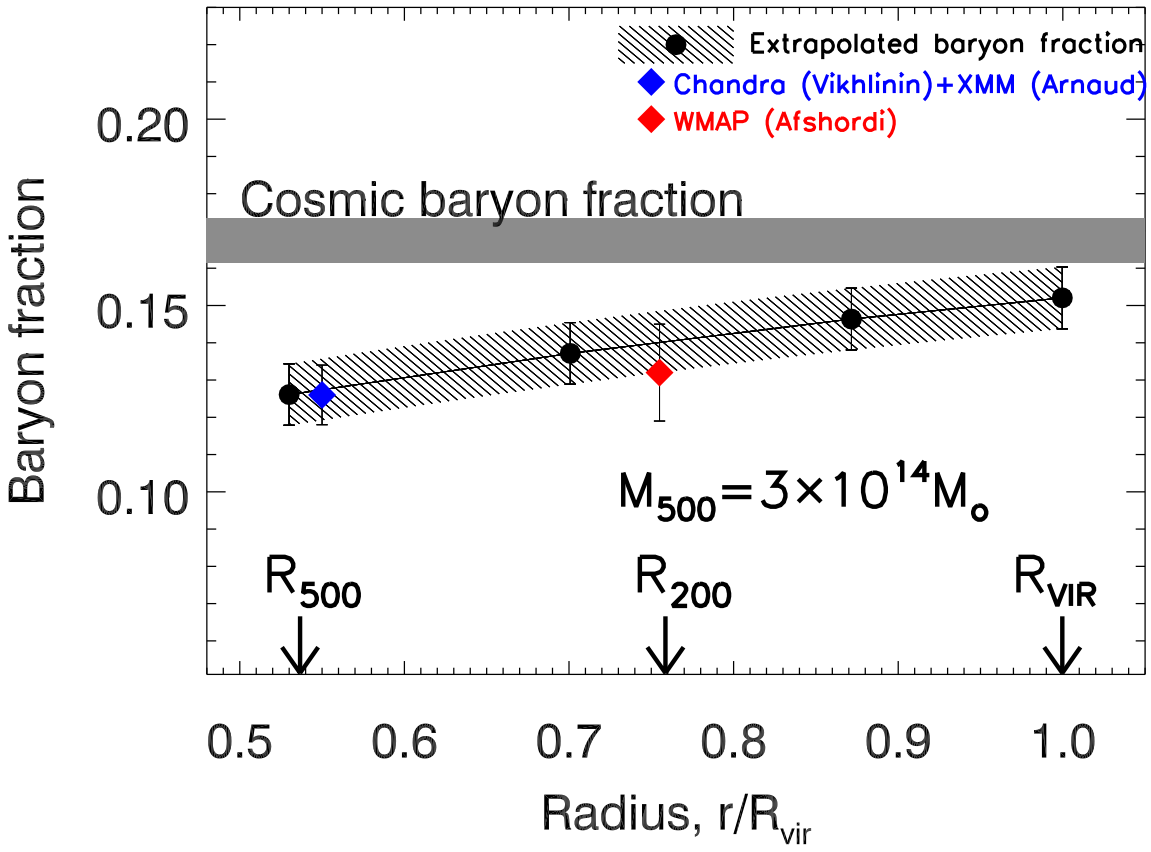

Figure 5.2: Comparison of extrapolated baryon fraction for $M_{500} \sim 3 \times 10^{14} M_{\odot}$, with observations from WMAP (Afshordi et al. [2007]). The gas fraction (empty points) from WMAP when corrected for the stellar fraction (filled points) (Giodini et al. [2009], Lin et al. [2003]) fits nicely with our extrapolated baryon fraction (shaded band), well within 1σ. The Chandra and XMM-Newton observations at R_{500} (Vikhlinin et al. [2006], Arnaud et al. [2007]) are also shown, which are the basis for our baseline gas fraction at R_{500}.

librium at outer radii. X-ray observations, which observe gas more directly than SZ-observations, show that gas profiles are more spread out than total mass profiles in clusters. We outlined various mechanisms which can cause such disruption of hydrostatic equilibrium at large radii. So a correct model for the gas density profile must allow for the gas to become slightly separated from the total matter profile.

Another reason for Komatsu et al. [2010]'s underestimation of the gas fraction could be an overestimation of the gas temperature at large radii. The SZ signal measures thermal pressure which is the product of gas density and temperature. The temperature profile may be the key to bridging the discrepancy between SZ and X-ray profiles.

Cluster temperature profiles have been observed in a number of studies to R_{200} or beyond, using Suzaku (George et al. [2009], Reiprich et al. [2009], Hoshino et al. [2010], Bautz et al. [2009]). George et al. [2009] observe the cluster PKS 0745-191 to nearly R_{100}. Excluding the core, they fit a power-law to the temperature decline: $T \propto r^{\alpha_T}$, where $\alpha_T = -0.94 \pm 0.06$. Bautz et al. [2009] observe the cluster Abell 1795 to close to R_{200} =200Mpc. They fit a power law to the temperature profile and find $\alpha_T = 0.9 \pm 0.3$, where the error is given at 90% confidence level. Vikhlinin et al. [2005] give temperature profiles for 13 clusters to R_{500} from Chandra data. A weighted mean of their temperature profile slopes is $\alpha_T = 0.45 \pm 0.05$. Reiprich et al. [2009] determine the temperature profile of Abell 2204 to R_{200} with Suzaku. The temperature rises steely near the center to $\sim$ 8keV and then drops to $\sim$ 4keV at R_{200}. The drop is by a factor of 0.6 from $0.3r_{200}$ to R_{200}, or roughly $\propto r^{-1}$. All together, observations indicate a power law index of the temperature profile between -0.4 and -1.0 at R_{200}. These and other measurements could be used to achieve better agreement between SZ decrements and X-ray measurements of the gas density profile.

Chapter 6

Conclusions

In this paper we address previous claims that clusters have a significant baryon deficiency with respect to the cosmic value of the baryon fraction. We use observations to extrapolate the observations of baryon fraction at R_{500} to the virial radius (R_{100}). We conclude that the baryon fraction in clusters rises at radii beyond R_{500} for all cluster masses. The baryon fraction in massive clusters ($M_{500} \sim 7 \times 10^{14} M_{\odot}$) reaches the cosmic value at $R_{vir} \pm 20\%$. The less massive clusters typically reach 75–85% of the cosmic baryon fraction at the virial radius. Variation in ICL or the relation of stellar fraction versus mass does not change our results significantly. We conclude that the baryon deficiency in clusters is less acute than previously described. We identify gravitational shock-heating, energy feedback from star formation, SNe and AGN, and energy transfer from dark matter as likely causes of the expansion of intracluster gas to large radii, whereas variation in star formation efficiency is a possible cause of variation of baryon fraction with mass. Comparisons with simulations show that these energetic mechanisms are able to explain our observations of baryon fraction in low-mass clusters. But simulations underpredict the baryon fraction for massive clusters. It remains unclear what mechanisms can raise the expected value of the baryon fraction in massive clusters to match observations.

Bibliography

N. Afshordi, Y.-T. Lin, and A. J. R. Sanderson. Wilkinson Microwave Anisotropy Probe Constraints on the Intracluster Medium. *ApJ*, 629:1–14, August 2005. doi: 10.1086/431274.

N. Afshordi, Y.-T. Lin, D. Nagai, and A. J. R. Sanderson. Missing thermal energy of the intracluster medium. *MNRAS*, 378:293–300, June 2007. doi: 10.1111/j.1365-2966.2007.11776.x.

S. W. Allen, R. W. Schmidt, and A. C. Fabian. Cosmological constraints from the X-ray gas mass fraction in relaxed lensing clusters observed with Chandra. *MNRAS*, 334:L11–L15, August 2002. doi: 10.1046/j.1365-8711.2002.05601.x.

S. Andreon. The stellar mass fraction and baryon content of galaxy clusters and groups. *ArXiv e-prints*, April 2010.

M. Arnaud, E. Pointecouteau, and G. W. Pratt. Calibration of the galaxy cluster M{500}-Y{X} relation with XMM-Newton. *A&A*, 474:L37–L40, November 2007. doi: 10.1051/0004-6361:20078541.

N. A. Bahcall. X-ray clusters of galaxies - Correlation of X-ray luminosity with galactic content. *ApJ*, 218:L93–L95, December 1977. doi: 10.1086/182583.

N. A. Bahcall and X. Fan. A Lightweight Universe? *Proceedings of the National Academy of Science*, 95:5956–5959, May 1998.

N. A. Bahcall, L. M. Lubin, and V. Dorman. Where is the Dark Matter? *ApJ*, 447: L81+, July 1995. doi: 10.1086/309577.

M. W. Bautz, E. D. Miller, J. S. Sanders, K. A. Arnaud, R. F. Mushotzky, F. S. Porter, K. Hayashida, J. P. Henry, J. P. Hughes, M. Kawaharada, K. Makashima, M. Sato, and T. Tamura. Suzaku Observations of Abell 1795: Cluster Emission to r_{200}. $PASJ, 61 : 1117 - -, October 2009$.

E. F. Bell and R. S. de Jong. Stellar Mass-to-Light Ratios and the Tully-Fisher Relation. *ApJ*, 550:212–229, March 2001. doi: 10.1086/319728.

B. A. Benson, S. E. Church, P. A. R. Ade, J. J. Bock, K. M. Ganga, C. N. Henson, and K. L. Thompson. Measurements of Sunyaev-Zel'dovich Effect Scaling Relations for Clusters of Galaxies. *ApJ*, 617:829–846, December 2004. doi: 10.1086/425677.

G. M. Bernstein, R. C. Nichol, J. A. Tyson, M. P. Ulmer, and D. Wittman. The Luminosity Function of the Coma Cluster Core for -25M/R-9.4. *AJ*, 110:1507–+, October 1995. doi: 10.1086/117624.

M. Birkinshaw. The Sunyaev-Zel'dovich effect. *Phys. Rep.*, 310:97–195, March 1999. doi: 10.1016/S0370-1573(98)00080-5.

P. Bode, J. P. Ostriker, and A. Vikhlinin. Exploring the Energetics of Intracluster Gas with a Simple and Accurate Model. *ApJ*, 700:989–999, August 2009. doi: 10.1088/0004-637X/700/2/989.

H. Boehringer, Y. Tanaka, R. F. Mushotzky, Y. Ikebe, and M. Hattori. An ASCA-ROSAT study of the distant, lensing cluster A 2390. *A&A*, 334:789–798, June 1998.

G. L. Bryan. Explaining the Entropy Excess in Clusters and Groups of Galaxies without Additional Heating. *ApJ*, 544:L1–L5, November 2000. doi: 10.1086/317289.

G. L. Bryan and M. L. Norman. Statistical Properties of X-Ray Clusters: Analytic and Numerical Comparisons. *ApJ*, 495:80–+, March 1998. doi: 10.1086/305262.

S. Burles and D. Tytler. Cosmological Deuterium Abundance and the Baryon Density of the Universe. *ArXiv Astrophysics e-prints*, March 1996.

R. G. Carlberg, H. K. C. Yee, E. Ellingson, R. Abraham, P. Gravel, S. Morris, and C. J. Pritchet. Galaxy Cluster Virial Masses and Omega. *ApJ*, 462:32–+, May 1996. doi: 10.1086/177125.

A. Cavaliere and R. Fusco-Femiano. The Distribution of Hot Gas in Clusters of Galaxies. *A&A*, 70:677–+, November 1978.

J. D. Cohn and M. White. The formation histories of galaxy clusters. *Astroparticle Physics*, 24:316–333, December 2005. doi: 10.1016/j.astropartphys.2005.07.006.

R. A. Crain, V. R. Eke, C. S. Frenk, A. Jenkins, I. G. McCarthy, J. F. Navarro, and F. R. Pearce. The baryon fraction of ΛCDM haloes. *MNRAS*, 377:41–49, May 2007. doi: 10.1111/j.1365-2966.2007.11598.x.

J. H. Croston, M. Arnaud, E. Pointecouteau, and G. W. Pratt. An improved deprojection and PSF-deconvolution technique for galaxy-cluster X-ray surface-brightness profiles. *A&A*, 459:1007–1019, December 2006. doi: 10.1051/0004-6361:20065795.

X. Dai, J. N. Bregman, C. S. Kochanek, and E. Rasia. On the Baryon Fractions in Clusters and Groups of Galaxies. *ArXiv e-prints*, November 2009.

L. P. David, C. Jones, and W. Forman. Cosmological implications of ROSAT observations of groups and clusters of galaxies. *ApJ*, 445:578–590, June 1995. doi: 10.1086/175722.

A. Dressler. A catalog of morphological types in 55 rich clusters of galaxies. *ApJS*, 42:565–609, April 1980. doi: 10.1086/190663.

J. Dubinski and R. G. Carlberg. The structure of cold dark matter halos. *ApJ*, 378: 496–503, September 1991. doi: 10.1086/170451.

V. R. Eke, S. Cole, and C. S. Frenk. Cluster evolution as a diagnostic for Omega. *MNRAS*, 282:263–280, September 1996.

V. R. Eke, J. F. Navarro, and C. S. Frenk. The Evolution of X-Ray Clusters in a Low-Density Universe. *ApJ*, 503:569–+, August 1998. doi: 10.1086/306008.

S. Ettori and I. Balestra. The outer regions of galaxy clusters: Chandra constraints on the X-ray surface brightness. *A&A*, 496:343–349, March 2009. doi: 10.1051/0004-6361:200811177.

A. E. Evrard. The intracluster gas fraction in X-ray clusters - Constraints on the clustered mass density. *MNRAS*, 292:289–+, December 1997.

O. Fakhouri and C.-P. Ma. The nearly universal merger rate of dark matter haloes in ΛCDM cosmology. *MNRAS*, 386:577–592, May 2008. doi: 10.1111/j.1365-2966.2008.13075.x.

J. J. Feldmeier, J. C. Mihos, H. L. Morrison, S. A. Rodney, and P. Harding. Deep CCD Surface Photometry of Galaxy Clusters. I. Methods and Initial Studies of Intracluster Starlight. *ApJ*, 575:779–800, August 2002. doi: 10.1086/341472.

J. J. Feldmeier, J. C. Mihos, H. L. Morrison, P. Harding, N. Kaib, and J. Dubinski. Deep CCD Surface Photometry of Galaxy Clusters. II. Searching for Intracluster Starlight in Non-cD clusters. *ApJ*, 609:617–637, July 2004. doi: 10.1086/421313.

A. Finoguenov, T. H. Reiprich, and H. Böhringer. Details of the mass-temperature relation for clusters of galaxies. *A&A*, 368:749–759, March 2001. doi: 10.1051/0004-6361:20010080.

M. R. George, A. C. Fabian, J. S. Sanders, A. J. Young, and H. R. Russell. X-ray observations of the galaxy cluster PKS0745-191: to the virial radius, and beyond. *MNRAS*, 395:657–666, May 2009. doi: 10.1111/j.1365-2966.2009.14547.x.

O. Gerhard, A. Kronawitter, R. P. Saglia, and R. Bender. Dynamical Family Properties and Dark Halo Scaling Relations of Giant Elliptical Galaxies. *AJ*, 121:1936–1951, April 2001. doi: 10.1086/319940.

S. Giodini, D. Pierini, A. Finoguenov, G. W. Pratt, H. Boehringer, A. Leauthaud, L. Guzzo, H. Aussel, M. Bolzonella, P. Capak, M. Elvis, G. Hasinger, O. Ilbert, J. S. Kartaltepe, A. M. Koekemoer, S. J. Lilly, R. Massey, H. J. McCracken, J. Rhodes, M. Salvato, D. B. Sanders, N. Z. Scoville, S. Sasaki, V. Smolcic, Y. Taniguchi, D. Thompson, and the COSMOS Collaboration. Stellar and Total Baryon Mass Fractions in Groups and Clusters Since Redshift 1. *ApJ*, 703:982–993, September 2009. doi: 10.1088/0004-637X/703/1/982.

A. H. Gonzalez, A. I. Zabludoff, D. Zaritsky, and J. J. Dalcanton. Measuring the Diffuse Optical Light in Abell 1651. *ApJ*, 536:561–570, June 2000. doi: 10.1086/308985.

A. H. Gonzalez, A. I. Zabludoff, and D. Zaritsky. Intracluster Light in Nearby Galaxy Clusters: Relationship to the Halos of Brightest Cluster Galaxies. *ApJ*, 618:195–213, January 2005. doi: 10.1086/425896.

A. H. Gonzalez, D. Zaritsky, and A. I. Zabludoff. A Census of Baryons in Galaxy Clusters and Groups. *ApJ*, 666:147–155, September 2007. doi: 10.1086/519729.

L. Grego, J. E. Carlstrom, M. K. Joy, E. D. Reese, G. P. Holder, S. Patel, A. R. Cooray, and W. L. Holzapfel. The Sunyaev-Zeldovich Effect in Abell 370. *ApJ*, 539:39–51, August 2000. doi: 10.1086/309190.

E. J. Hallman, J. O. Burns, P. M. Motl, and M. L. Norman. The β-Model Problem: The Incompatibility of X-Ray and Sunyaev-Zeldovich Effect Model Fitting for Galaxy Clusters. *ApJ*, 665:911–920, August 2007. doi: 10.1086/519447.

N. W. Halverson, T. Lanting, P. A. R. Ade, K. Basu, A. N. Bender, B. A. Benson, F. Bertoldi, H.-M. Cho, G. Chon, J. Clarke, M. Dobbs, D. Ferrusca, R. Güsten, W. L. Holzapfel, A. Kovács, J. Kennedy, Z. Kermish, R. Kneissl, A. T. Lee, M. Lueker, J. Mehl, K. M. Menten, D. Muders, M. Nord, F. Pacaud, T. Plagge, C. Reichardt, P. L. Richards, R. Schaaf, P. Schilke, F. Schuller, D. Schwan, H. Spieler, C. Tucker, A. Weiss, and O. Zahn. Sunyaev-Zel'Dovich Effect Observations of the Bullet Cluster (1E 0657-56) with APEX-SZ. *ApJ*, 701:42–51, August 2009. doi: 10.1088/0004-637X/701/1/42.

A. Hoshino, J. P. Henry, K. Sato, H. Akamatsu, W. Yokota, S. Sasaki, Y. Ishisaki, T. Ohashi, M. Bautz, Y. Fukazawa, N. Kawano, A. Furuzawa, K. Hayashida, T. Tawa, J. Hughes, M. Kokubun, and T. Tamura. X-ray Temperature and Mass Measurements to the Virial Radius of Abell 1413 with Suzaku. *ArXiv e-prints*, January 2010.

N. Itoh, S. Nozawa, Y. Kawana, and Y. Kohyama. Relativistic Corrections to the Sunyaev-Zeldovich Effect for Clusters of Galaxies. IV. Analytic Fitting Formula for the Numerical Results. *ApJ*, 536:31–35, June 2000. doi: 10.1086/308938.

N. Jarosik, C. L. Bennett, J. Dunkley, B. Gold, M. R. Greason, M. Halpern, R. S. Hill, G. Hinshaw, A. Kogut, E. Komatsu, D. Larson, M. Limon, S. S. Meyer, M. R. Nolta, N. Odegard, L. Page, K. M. Smith, D. N. Spergel, G. S. Tucker, J. L. Weiland, E. Wollack, and E. L. Wright. Seven-Year Wilkinson Microwave Anisotropy Probe (WMAP) Observations: Sky Maps, Systematic Errors, and Basic Results. *ArXiv e-prints*, January 2010.

E. Komatsu and U. Seljak. Universal gas density and temperature profile. *MNRAS*, 327:1353–1366, November 2001. doi: 10.1046/j.1365-8711.2001.04838.x.

E. Komatsu, K. M. Smith, J. Dunkley, C. L. Bennett, B. Gold, G. Hinshaw, N. Jarosik, D. Larson, M. R. Nolta, L. Page, D. N. Spergel, M. Halpern, R. S. Hill, A. Kogut, M. Limon, S. S. Meyer, N. Odegard, G. S. Tucker, J. L. Weiland, E. Wollack, and E. L. Wright. Seven-Year Wilkinson Microwave Anisotropy Probe (WMAP) Observations: Cosmological Interpretation. *ArXiv e-prints*, January 2010.

J. E. Krick and R. A. Bernstein. Diffuse Optical Light in Galaxy Clusters. II. Correlations with Cluster Properties. *AJ*, 134:466–493, August 2007. doi: 10.1086/518787.

Y.-T. Lin, J. J. Mohr, and S. A. Stanford. Near-Infrared Properties of Galaxy Clusters: Luminosity as a Binding Mass Predictor and the State of Cluster Baryons. *ApJ*, 591:749–763, July 2003. doi: 10.1086/375513.

R. Mandelbaum, U. Seljak, and C. M. Hirata. A halo massconcentration relation from weak lensing. *Journal of Cosmology and Astro-Particle Physics*, 8:6–+, August 2008. doi: 10.1088/1475-7516/2008/08/006.

M. Markevitch, W. R. Forman, C. L. Sarazin, and A. Vikhlinin. The Temperature Structure of 30 Nearby Clusters Observed with ASCA: Similarity of Temperature Profiles. *ApJ*, 503:77–+, August 1998. doi: 10.1086/305976.

I. G. McCarthy, R. G. Bower, and M. L. Balogh. Revisiting the baryon fractions of galaxy clusters: a comparison with WMAP 3-yr results. *MNRAS*, 377:1457–1463, June 2007. doi: 10.1111/j.1365-2966.2007.11733.x.

C. A. Metzler and A. E. Evrard. A simulation of the intracluster medium with feedback from cluster galaxies. *ApJ*, 437:564–583, December 1994. doi: 10.1086/175022.

G. Murante, M. Giovalli, O. Gerhard, M. Arnaboldi, S. Borgani, and K. Dolag. The importance of mergers for the origin of intracluster stars in cosmological simulations of galaxy clusters. *MNRAS*, 377:2–16, May 2007. doi: 10.1111/j.1365-2966.2007.11568.x.

D. Nagai, A. V. Kravtsov, and A. Vikhlinin. Effects of Galaxy Formation on Thermodynamics of the Intracluster Medium. *ApJ*, 668:1–14, October 2007. doi: 10.1086/521328.

J. F. Navarro, C. S. Frenk, and S. D. M. White. Simulations of X-ray clusters. *MNRAS*, 275:720–740, August 1995.

J. F. Navarro, C. S. Frenk, and S. D. M. White. The Structure of Cold Dark Matter Halos. *ApJ*, 462:563–+, May 1996. doi: 10.1086/177173.

A. F. Neto, L. Gao, P. Bett, S. Cole, J. F. Navarro, C. S. Frenk, S. D. M. White, V. Springel, and A. Jenkins. The statistics of Λ CDM halo concentrations. *MNRAS*, 381:1450–1462, November 2007. doi: 10.1111/j.1365-2966.2007.12381.x.

T. Plagge, B. A. Benson, P. A. R. Ade, K. A. Aird, L. E. Bleem, J. E. Carlstrom, C. L. Chang, H. -. Cho, T. M. Crawford, A. T. Crites, T. de Haan, M. A. Dobbs, E. M. George, N. R. Hall, N. W. Halverson, G. P. Holder, W. L. Holzapfel, J. D. Hrubes, M. Joy, R. Keisler, L. Knox, A. T. Lee, E. M. Leitch, M. Lueker, D. Marrone, J. J. McMahon, J. Mehl, S. S. Meyer, J. J. Mohr, T. E. Montroy, S. Padin, C. Pryke, C. L. Reichardt, J. E. Ruhl, K. K. Schaffer, L. Shaw, E. Shirokoff, H. G. Spieler, B. Stalder, Z. Staniszewski, A. A. Stark, K. Vanderlinde, J. D. Vieira, R. Williamson, and O. Zahn. Sunyaev-Zel'dovich Cluster Profiles Measured with the South Pole Telescope. *ArXiv e-prints*, November 2009.

E. Pointecouteau, M. Arnaud, and G. W. Pratt. The structural and scaling properties

of nearby galaxy clusters. I. The universal mass profile. *A&A*, 435:1–7, May 2005. doi: 10.1051/0004-6361:20042569.

G. W. Pratt, M. Arnaud, and E. Pointecouteau. Structure and scaling of the entropy in nearby galaxy clusters. *A&A*, 446:429–438, February 2006. doi: 10.1051/0004-6361:20054025.

G. W. Pratt, J. H. Croston, M. Arnaud, and H. Böhringer. Galaxy cluster X-ray luminosity scaling relations from a representative local sample (REXCESS). *A&A*, 498:361–378, May 2009. doi: 10.1051/0004-6361/200810994.

C. W. Purcell, J. S. Bullock, and A. R. Zentner. The metallicity of diffuse intrahalo light. *MNRAS*, 391:550–558, December 2008. doi: 10.1111/j.1365-2966.2008.13938.x.

E. D. Reese, J. E. Carlstrom, M. Joy, J. J. Mohr, L. Grego, and W. L. Holzapfel. Determining the Cosmic Distance Scale from Interferometric Measurements of the Sunyaev-Zeldovich Effect. *ApJ*, 581:53–85, December 2002. doi: 10.1086/344137.

T. H. Reiprich, D. S. Hudson, Y.-Y. Zhang, K. Sato, Y. Ishisaki, A. Hoshino, T. Ohashi, N. Ota, and Y. Fujita. Suzaku measurement of Abell 2204's intracluster gas temperature profile out to 1800 kpc. *A&A*, 501:899–905, July 2009. doi: 10.1051/0004-6361/200810404.

A. J. R. Sanderson, T. J. Ponman, A. Finoguenov, E. J. Lloyd-Davies, and M. Markevitch. The Birmingham-CfA cluster scaling project - I. Gas fraction and the M-T$_X$ $relation.$ $MNRAS, 340 : 989 - -1010, April 2003.$ $doi : 10.1046/j.1365 - 8711.2003.06401.x.$

E. S. Sheldon, D. E. Johnston, R. Scranton, B. P. Koester, T. A. McKay, H. Oyaizu, C. Cunha, M. Lima, H. Lin, J. A. Frieman, R. H. Wechsler, J. Annis, R. Mandelbaum, N. A. Bahcall, and M. Fukugita. Cross-correlation Weak Lensing of

SDSS Galaxy Clusters. I. Measurements. *ApJ*, 703:2217–2231, October 2009. doi: 10.1088/0004-637X/703/2/2217.

D. Sijacki, C. Pfrommer, V. Springel, and T. A. Enßlin. Simulations of cosmic-ray feedback by active galactic nuclei in galaxy clusters. *MNRAS*, 387:1403–1415, July 2008. doi: 10.1111/j.1365-2966.2008.13310.x.

V. Springel and L. Hernquist. The history of star formation in a Λ cold dark matter universe. *MNRAS*, 339:312–334, February 2003. doi: 10.1046/j.1365-8711.2003.06207.x.

M. Sun, G. M. Voit, M. Donahue, C. Jones, W. Forman, and A. Vikhlinin. Chandra Studies of the X-Ray Gas Properties of Galaxy Groups. *ApJ*, 693:1142–1172, March 2009. doi: 10.1088/0004-637X/693/2/1142.

M. Takizawa and S. Mineshige. Evolution of X-Ray Clusters of Galaxies and Shock Heating of the Intracluster Medium. *ApJ*, 499:82–+, May 1998. doi: 10.1086/305598.

P. Tozzi and C. Norman. The Evolution of X-Ray Clusters and the Entropy of the Intracluster Medium. *ApJ*, 546:63–84, January 2001. doi: 10.1086/318237.

K. Umetsu, M. Birkinshaw, G.-C. Liu, J.-H. P. Wu, E. Medezinski, T. Broadhurst, D. Lemze, A. Zitrin, P. T. P. Ho, C.-W. L. Huang, P. M. Koch, Y.-W. Liao, K.-Y. Lin, S. M. Molnar, H. Nishioka, F.-C. Wang, P. Altamirano, C.-H. Chang, S.-H. Chang, S.-W. Chang, M.-T. Chen, C.-C. Han, Y.-D. Huang, Y.-J. Hwang, H. Jiang, M. Kesteven, D. Y. Kubo, C.-T. Li, P. Martin-Cocher, P. Oshiro, P. Raffin, T. Wei, and W. Wilson. Mass and Hot Baryons in Massive Galaxy Clusters from Subaru Weak-Lensing and AMiBA Sunyaev-Zel'Dovich Effect Observations. *ApJ*, 694: 1643–1663, April 2009. doi: 10.1088/0004-637X/694/2/1643.

R. Valdarnini. Iron abundances and heating of the intracluster medium in hydrodynamical simulations of galaxy clusters. *MNRAS*, 339:1117–1134, March 2003. doi: 10.1046/j.1365-8711.2003.06163.x.

A. Vikhlinin, M. Markevitch, S. S. Murray, C. Jones, W. Forman, and L. Van Speybroeck. Chandra Temperature Profiles for a Sample of Nearby Relaxed Galaxy Clusters. *ApJ*, 628:655–672, August 2005. doi: 10.1086/431142.

A. Vikhlinin, A. Kravtsov, W. Forman, C. Jones, M. Markevitch, S. S. Murray, and L. Van Speybroeck. Chandra Sample of Nearby Relaxed Galaxy Clusters: Mass, Gas Fraction, and Mass-Temperature Relation. *ApJ*, 640:691–709, April 2006. doi: 10.1086/500288.

G. M. Voit and G. L. Bryan. On the Distribution of X-Ray Surface Brightness from Diffuse Gas. *ApJ*, 551:L139–L142, April 2001. doi: 10.1086/320020.

G. M. Voit, G. L. Bryan, M. L. Balogh, and R. G. Bower. Modified Entropy Models for the Intracluster Medium. *ApJ*, 576:601–624, September 2002. doi: 10.1086/341864.

T. P. Walker, G. Steigman, H.-S. Kang, D. M. Schramm, and K. A. Olive. Primordial nucleosynthesis redux. *ApJ*, 376:51–69, July 1991. doi: 10.1086/170255.

D. A. White and A. C. Fabian. Einstein Observatory evidence for the widespread baryon overdensity in clusters of galaxies. *MNRAS*, 273:72–84, March 1995.

S. D. M. White, J. F. Navarro, A. E. Evrard, and C. S. Frenk. The baryon content of galaxy clusters: a challenge to cosmological orthodoxy. *Nature*, 366:429–433, December 1993. doi: 10.1038/366429a0.

Y.-Y. Zhang, A. Finoguenov, H. Böhringer, J.-P. Kneib, G. P. Smith, R. Kneissl, N. Okabe, and H. Dahle. LoCuSS: comparison of observed X-ray and lensing

galaxy cluster scaling relations with simulations. *A&A*, 482:451–472, May 2008. doi: 10.1051/0004-6361:20079103.

S. Zibetti. Statistical Properties of the IntraCluster Light from SDSS Image Stacking. In J. Davies & M. Disney, editor, *IAU Symposium*, volume 244 of *IAU Symposium*, pages 176–185, May 2008. doi: 10.1017/S174392130701397X.

F. Zwicky. On the Masses of Nebulae and of Clusters of Nebulae. *ApJ*, 86:217–+, October 1937. doi: 10.1086/143864.